Recovery strategies to cope with micrometeoroid impacts in the LISA mission

Acta Astronautica 211 (2023) 844–864

Contents lists available at ScienceDirect

Acta Astronautica

journal homepage: www.elsevier.com/locate/actaastro

Recovery strategies to cope with micrometeoroid impacts in the LISA mission

Carlo Novara [a], Mario Virdis [a], Michele Pagone [a,*], Dario Ruggiero [b], Elisa Capello [b], Elisabetta Punta [c], Sabrina Dionisio [d], Simone Vidano [d], Jonathan Grzymisch [e], Valentin Preda [e]

[a] Department of Electronics and Telecommunications, Politecnico di Torino, Corso Duca degli Abruzzi, 24, 10129, Turin, Italy
[b] Department of Mechanical and Aerospace Engineering, Politecnico di Torino, Corso Duca degli Abruzzi, 24, 10129, Turin, Italy
[c] Institute of Electronics, Information Engineering and Telecommunications (IEIIT), DIITET, Consiglio Nazionale delle Ricerche (CNR), Politecnico di Torino, Corso Duca degli Abruzzi, 24, 10129, Turin, Italy
[d] Thales Alenia Space Italy, Strada Antica di Collegno, 253, 10146, Torino, Italy
[e] Guidance, Navigation, and Control Section (TEC-SAG), ESTEC, European Space Agency, Kepleralaan 1, Noordwijk, 2201 AZ, the Netherlands

ARTICLE INFO

Keywords:
LISA
GNC
Meteoroids
Monte Carlo
Observer
Spacecraft

ABSTRACT

We propose an analysis of the recovery strategies for the science mode of the Laser Interfer-ometer Space Antenna (LISA) mission after a meteoroid impacts the spacecraft. The mission consists of a three-spacecraft constellation traveling in a heliocentric orbit, detecting gravitational waves through laser interferometry. To this end, each spacecraft must travel in a free-fall condition in order to reject any possible disturbance and noise affecting the control loop. Nevertheless, if one of the three satellites crosses a meteoroids stream, the collisions can produce attitude perturbations that must be compensated by the control loop. Indeed, in this latter case, the interferometer laser links can be lost. Unfortunately, the link recovery is accomplished through a quite time-consuming re-acquisition maneuver, implying a significant reduction of the science mode time. For this reason, we propose different strategies for a fast recovery of the nominal attitude. The strategies are supported and traded-off by means of extensive simulations, including a Monte Carlo campaign and a worst-case analysis.

1. Introduction

LISA is one of the next large-class missions from the European Space Agency (ESA), expected to be launched in 2034 [1,2]. The mission is intended to detect, from orbit, perturbations of the space-time curvature due to gravitational waves, through a space-based interferometer [3]. In detail, the LISA mission consists of a constellation composed of three different satellites forming a triangle in heliocentric orbit. Each satellite of the constellation is approximately $2.5 \cdot 10^6$ km from the other two. In order to observe gravitational waves, each probe of the constellation is equipped with two different cubic test masses (TMs) moving in free fall condition, inside an electrostatic suspension. The detection of the gravity perturbations consists of identifying the space-time grid deformation by measuring the relative distance between the two far TMs, belonging to two different spacecraft (SC) of the constellation [4]. Indeed, the TM free-fall condition is performed [5] by compensating and rejecting any possible noise and disturbance, so that the residual attitude and position jitters of the TMs can fulfill tight requirements at the nanoscopic level [6–8].

Nevertheless, as experienced by the prototype LISA pathfinder mission [9–11], when the constellation crosses a meteoroid stream, some serious issues may arise. Indeed, if a collision with a meteoroid happens, the impact may affect the science mode by causing position and attitude perturbations of the spacecrafts relative to the TMs (see, e.g. Refs. [12,13]). As already mentioned, the LISA mission must guarantee a high level of performance in terms of tracking requirements, in order to establish the link connection between the lasers emitted by two different spacecraft [14]. Hence, even small collisions may cause a sufficiently high attitude perturbation causing a loss of the laser link. When this occurs, the LISA mission is already able to perform a re-acquisition scanning spiral maneuver [15], which, however, is quite time consuming, with a consequent reduction of time spent in the science mode. Another issue related to the micrometeoroid impact regards the high attitude and position perturbation that can make the TMs escape from the electrostatic control. In order to avoid this phenomena, it is required to re-grab them by switching the operating mode in order to deliver a higher control authority [16].

* Corresponding author.
E-mail addresses: carlo.novara@polito.it (C. Novara), michele.pagone@polito.it (M. Pagone).

https://doi.org/10.1016/j.actaastro.2023.06.031
Received 11 October 2022; Received in revised form 7 June 2023; Accepted 17 June 2023
Available online 13 July 2023

Acronym and abbreviations

CAS	Constellation Acquisition Sensor CRF: Constellation Reference Frame
DFACS	Drag-Free Attitude Control System DWS: Differential Wavefront Sensing
ESA	European Space Agency
GNC	Guidance, Navigation, and Control GRS: Gravitational Reference Sensor
HR	High Resolution
IRF	Inertial Reference Frame
LISA	Laser Interferometer Space Antenna MC: Monte Carlo
MPS	Micro Propulsion System
NUMES	New Mission End-to-End Simulator OA: Optical Assembly
ORF	Optical Reference Frame PD: Proportional Derivative
PID	Proportional Integral Derivative SC: Spacecraft
SMO	Sliding Model Observer
SRF	Spacecraft Reference Frame TM: Test Mass
TMRF	Test Mass Reference Frame

In this paper, the effects of the micrometeoroid impacts are addressed. A micrometeoroid is a small particle of rock, usually lighter than a gram. In control design, generally, micrometeoroid impact is considered as an external disturbance for the closed loop system, and, usually, the order of magnitude is negligible with respect to other sources of disturbances (see, e.g. Ref. [17]). As discussed in Refs. [18, 19], hypervelocity impacts may have enough energy to damage the spacecraft, generating non-negligible disturbances. A study on the effect of this kind of impacts for the LISA spacecraft is addressed in Ref. [20]. The data on the micrometeoroid impacts have been provided by the European Space Agency. Here, we model the micrometeroid impact by using a rectangular force and torque steps of short duration that account for the linear and angular momentum transferred during the collision. Impacts with different features, in terms of linear and angular momentum direction and magnitude, are considered. We observe that, in the case of strong impacts, the attitude perturbation is so high that the laser beams can actually exceed the receiving sensor range. Then, a control strategy for a fast recovery of the constellation is designed by developing an impact detector based on a state observer that changes the operating mode from the drag-free to recovery mode. The guidance and the controller are changed accordingly.

Therefore, the main purpose of this paper is to design and test some recovery strategies for fast and accurate re-acquisition of the nominal attitude of the constellation, without performing a time-consuming scanning spiral maneuver. The problem of constellation re-orientation has been widely discussed and studied in recent years, and many approaches are available in the literature (see, e.g. Refs. [21–23]), together with fault-tolerant orbit and attitude controllers [24–29]. This paper is mainly devoted to developing three aspects of the recovery guidance, navigation, and control (GNC): i) an impact detector, which is in charge of switching the GNC from the science to the recovery mode, and vice-versa; ii) the design of a proper navigation algorithm that is able to efficiently reject the external disturbances, allowing a fast and accurate estimation of the spacecraft state (see, e. g, Refs. [30–33]); iii) the design of a controller able to recover the nominal spacecraft attitude and TMs position.

The LISA system has been simulated by means of the nonlinear mathematical dynamics developed in Ref. [7] and then implemented in the Matlab/Simulink environment. The simulator includes the noises affecting the actuators and the sensors during the science phase of the mission. Moreover, non-Keplerian forces are also accounted for, like the solar pressure and the TMs self-gravity forces (i.e., the force generated by the spacecraft on the TM). This simulator has been employed for tuning the parameters of the navigation and control modules. Moreover, the Thales Alenia Space high-fidelity simulator [34] has been used for the numerical analysis presented in this paper, including a Monte Carlo (MC) campaign, as well as, a stress test. This simulator also includes the scheduling of the command of nine independent thrusters composing the micro propulsion system (MPS), as well as, the internal thruster dynamics.

2. Spacecraft model

In this section, some of the most relevant aspects of the mathematical model of the LISA spacecraft are presented. Note that the complete nonlinear mathematical model was developed and validated in Ref. [7]. All the figures regarding the model are taken from Ref. [7]. Note also that all the reference frames used in the following subsections are explained in detail in Appendix A.

A sketch of the spacecraft is shown in Fig. 1a, where the test mass and the optical assemblies (OAs) with the lasers can be seen. Also, a schema of the constellation orbiting the sun is shown in Fig. 1b.

During the LISA mission phases, there are different sets of sensors available, thus, different quantities can be measured, with different accuracy. In this part, the focus is put on the drag-free phase. Thus, when necessary, the operating conditions that characterize the sensors and actuators during that mission phase are assumed.

2.1. Drag-free tasks

During the drag-free phase the controller should be able to perform the following tasks:

- *Maintain the laser links*: controlling the attitude of the spacecraft and the telescopes' inter-angle in a way that keeps the incoming lasers at the centers of the laser sensors and the outgoing lasers on the centers of the laser sensors on the other spacecraft.
- *Control the TM position*: the controller has to keep the TMs at the center of their housings, also called cages. This is achieved by moving the spacecraft around the TM using the MPS and by directly affecting the single TM independently by means of the electrodes in the cages. Note that a specific more stringent performance is required for position control along the drag-free direction.
- *Control the TM attitude*: the controller has to regulate the TM cube attitude so that the laser can reflect off its surface properly.

The aforementioned requirements make the following quantities relevant for the control algorithm:

- $\mathbf{q}_{\mathrm{SC}}$: the attitude error of the SC with respect to the constellation frame.
- $\boldsymbol{r}_{\mathrm{m1o1}}$ and $\boldsymbol{r}_{\mathrm{m2o2}}$: the position of the TMs with respect to the respective cage centers, in optical reference frames (ORF) coordinates.
- $\mathbf{q}_{\mathrm{m1o1}}$ and $\mathbf{q}_{\mathrm{m2o2}}$: the TMs' attitudes with respect to their ORF.
- ξ_1 and ξ_2: the rotation angles of the two OAs with respect to their nominal positions.

These quantities can be obtained in different ways:

- $\mathbf{q}_{\mathrm{SC}}$ can be locally reconstructed starting by the SC–SC differential wavefront sensing (DWS) measured angles, that allow for the reconstruction of the constellation reference frame (CRF).
- $\boldsymbol{r}_{\mathrm{m1o1}}$ and $\boldsymbol{r}_{\mathrm{m2o2}}$ can be completely measured by the gravitational reference sensor (GRS) or partially (only x–axis) by the local SC–TM interferometer.
- $\mathbf{q}_{\mathrm{m1o1}}$ and $\mathbf{q}_{\mathrm{m2o2}}$ can be completely measured by the GRS or partially (pitch and yaw) by the SC–TM DWS.
- ξ_1 and ξ_2 are assumed to be directly measured.

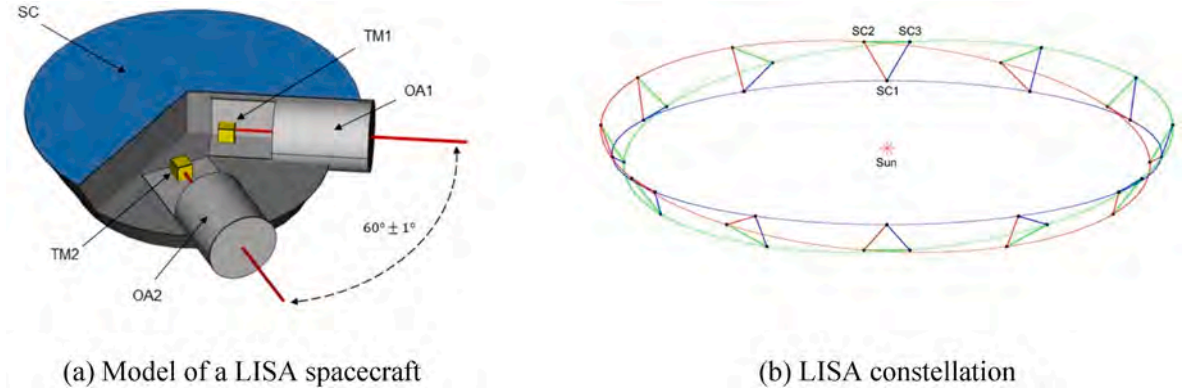

(a) Model of a LISA spacecraft (b) LISA constellation

Fig. 1. Lisa system.

2.2. Spacecraft attitude

In order to maintain both laser links during orbit, the SC attitude should follow the constellation attitude as close as possible. This is achieved by driving the quaternion $\mathbf{q}_{\mathrm{SC}}$, representing the error between the SC attitude and the constellation attitude, to zero. Hence the attitude error dynamics are given by

$$\dot{\boldsymbol{q}}_{sc} = \frac{\mathbf{1}}{\mathbf{2}}\, \boldsymbol{q}_{\mathrm{SC}} \otimes [\mathbf{0} \quad \boldsymbol{\omega}_{\mathrm{S}}]^{T}, \tag{1}$$

$$\dot{\boldsymbol{\omega}}_{\mathbf{SC}} = \dot{\boldsymbol{\omega}}_{\mathbf{SI}} - \dot{\boldsymbol{\omega}}_{\mathbf{CI}} + \boldsymbol{\omega}_{\mathrm{S}} \times \mathrm{T}_{\mathrm{C}}^{\mathrm{S}}\, \boldsymbol{\omega}_{\mathrm{C}}, \tag{2}$$

$$\begin{aligned}\dot{\boldsymbol{\omega}}_{\mathbf{SI}} = {} & -\mathrm{J}_{\mathrm{S}}^{-1}\, \boldsymbol{\omega}_{\mathrm{S}} \times (\mathrm{J}_{\mathrm{S}}\, \boldsymbol{\omega}_{\mathrm{S}}) + \mathrm{J}_{\mathrm{S}}^{-1} \left(M_{\mathrm{T}} + D_{\mathrm{T}} + D_{\odot \mathrm{press}} + M_{\mathrm{met}}\right) \\ & + -\mathrm{J}_{\mathrm{S}}^{-1} \sum_{j=1,2} \mathrm{T}_{\mathrm{o}_j}^{\mathrm{S}}\, \mathrm{I}_{zz}\, \ddot{\boldsymbol{\xi}}_j + \mathrm{T}_{\mathrm{o}_j}^{\mathrm{S}}\, M_{\mathrm{E}_j} + \boldsymbol{b}_j \times \left(\mathrm{T}_{\mathrm{o}_j}^{\mathrm{S}}\, F_{\mathrm{E}_j}\right),\end{aligned} \tag{3}$$

$$\mathrm{T}_{\mathrm{C}}^{\mathrm{S}} = \mathrm{R}\left(q_{\mathrm{SC}}^{*}\right), \tag{4}$$

$$\mathrm{T}_{\mathrm{o}_1}^{\mathrm{S}} = \mathrm{R}_z\left(\frac{\pi}{6} + \xi_1\right), \tag{5}$$

$$\mathrm{T}_{\mathrm{o}_2}^{\mathrm{S}} = \mathrm{R}_z\left(-\frac{\pi}{6} + \xi_2\right), \tag{6}$$

where:

- J_{S} is the SC inertia matrix with respect to the spacecraft reference frame (SRF);
- $\mathbf{M}_{\mathrm{T}}$ is the torque provided by the thrusters, that is given in SRF coordinates;
- $\mathbf{D}_{\mathrm{T}}$ is the torque noise of the thrusters;
- $\mathbf{D}_{\odot \mathrm{press}}$ is the torque from solar radiation pressure;
- $\mathbf{M}_{\mathrm{met}}$ is the torque exerted by the meteoroid impact onto the SC;
- I_{zz} is the inertia of both OAs along the z–axis, that passes through the pivot point;
- $\boldsymbol{\xi}_j \in \mathrm{R}^3$ is the rotation vector that represents the rotation of the j-th OA, expressed in the ORF: $\boldsymbol{\xi}_j = [0\ 0\ \xi_j]^{\top}$;
- $\mathbf{M}_{\mathrm{E}j}$ is the torque generated by the j-th GRS electrodes on the j-th TM, in ORF coordi-nates;
- $\mathbf{F}_{\mathrm{E}j}$ is the force applied by the j-th GRS electrodes on the j-th TM, in ORF coordinates;
- $\boldsymbol{b}_j$ is the position with respect to the SC CoM (the SRF origin) of the cage center of the j-th GRS;

- $\mathrm{T}_{\mathrm{C}}^{\mathrm{S}}$ is a coordinate transformation matrix from the constellation reference frame to the spacecraft reference frame;
- $\mathrm{T}_{\mathrm{o}_i}^{\mathrm{S}}$ are coordinate transformation matrices, that convert coordinates from the i-th optical reference frame to the spacecraft reference frame.

2.3. Optical assembly rotation

Another task that the controller needs to carry out in order to keep the laser link active is the breathing of the OAs inter-angle. The internal angles of the triangular formation varies of approximately $\pm 1^{\circ}$ per year, due to the particular orbital dynamics. The rotation dynamics is relative to the OA's nominal position. Hence, the attitude of the OAs is described by:

$$\ddot{\boldsymbol{\xi}}_{\mathbf{o_j}} = \frac{\mathbf{1}}{\mathrm{I}_{zz}} \left(\boldsymbol{M}_{\mathrm{OA}_j} + \boldsymbol{D}_{\xi_j} - \boldsymbol{M}_{\mathrm{E}_j}\right) - \mathrm{T}_{\mathrm{S}}^{o_j}\, \dot{\boldsymbol{\omega}}_{\mathbf{SI}} - \frac{\boldsymbol{\beta}}{\mathrm{I}_{zz}} \dot{\boldsymbol{\xi}}_{\mathbf{o_j}} - \frac{\mathrm{k}_{\xi}}{\mathrm{I}_{zz}} \boldsymbol{\xi}_{\mathrm{o}_j}, \tag{7}$$

$$\mathrm{T}_{\mathrm{S}}^{\mathrm{o}_1} = \mathrm{T}_{\mathrm{o}_1}^{\mathrm{S}^{\top}} = \mathrm{R}_z\left(-\frac{\pi}{6} - \xi_1\right), \tag{8}$$

$$\mathrm{T}_{\mathrm{S}}^{\mathrm{o}_2} = \mathrm{T}_{\mathrm{o}_2}^{\mathrm{S}^{\top}} = \mathrm{R}_z\left(\frac{\pi}{6} - \xi_2\right). \tag{9}$$

2.4. Test mass attitude

The TM attitude is controlled by means of the GRS electrodes. It is important to keep the TM aligned with the cage frame in order to let the lasers properly reflect off its front surface.

As for the SC attitude case, this latter task is achieved by regulating the relative attitude $\mathbf{q}_{\mathrm{m}_j}$ to zero. This quantity represents the relative attitude of the single TM with respect to the relevant cage frame.

Therefore, the TM attitude dynamics is described as

$$\dot{\mathbf{q}}_{mj} = \frac{\mathbf{1}}{\mathbf{2}}\, \boldsymbol{q}_{\mathrm{m}_j} \otimes \begin{bmatrix} \mathbf{0} \\ \boldsymbol{\omega}_{\boldsymbol{mj}} \end{bmatrix}, \tag{10}$$

$$\dot{\omega}_{\mathrm{m}_{\mathrm{o}_j}} = \dot{\omega}_{\mathrm{m}_j\mathrm{I}} - \mathrm{T}_{\mathrm{o}_j}^{\mathrm{m}_j} \dot{\xi}_{\mathrm{o}_j} - \mathrm{T}_{\mathrm{S}}^{\mathrm{m}_j}\, \dot{\omega}_{\mathrm{SI}} + \omega_{\mathrm{m}_{\mathrm{o}_j}} \times \mathrm{T}_{\mathrm{o}_j}^{\mathrm{m}_j} \dot{\xi}_{\mathrm{o}_j} + \omega_{\mathrm{m}_j\mathrm{I}} \times \mathrm{T}_{\mathrm{S}}^{\mathrm{m}_j}\, \omega_{\mathrm{S}}, \tag{11}$$

$$\dot{\omega}_{\mathrm{m}_j\mathrm{I}} = \mathrm{J}_{\mathrm{m}_j}^{-1}\, \mathrm{T}_{\mathrm{o}_j}^{\mathrm{m}_j} \left(M_{\mathrm{E}_j} + D_{\mathrm{E}_j}\right) - \mathrm{J}_{\mathrm{m}_j}^{-1} \omega_{\mathrm{m}_j\mathrm{I}} \times \left(\mathrm{J}_{\mathrm{m}_j} \boldsymbol{\omega}_{\mathrm{m}_j\mathrm{I}}\right), \tag{12}$$

$$\mathrm{T}_{\mathrm{o}_j}^{\mathrm{m}_j} = \mathrm{R}\left(q_{\mathrm{m}_j}^{*}\right), \tag{13}$$

$$\mathrm{T}_{\mathrm{S}}^{\mathrm{m}_j} = \mathrm{T}_{\mathrm{o}_j}^{\mathrm{m}_j}\, \mathrm{T}_{\mathrm{S}}^{\mathrm{o}_j}, \tag{14}$$

where:

- $\boldsymbol{\omega}_{\mathrm{mj\ oj}}$ is the angular velocity of the j-th TM with respect to the j-th optical reference frame;
- $\boldsymbol{\omega}_{\mathrm{mj\ I}}$ is the angular velocity of the j-th TM with respect to the inertial reference frame;
- $\mathbf{M}_{\mathrm{E}j}$ is the torque provided by the electrodes around the j-th TM cage;
- $\mathbf{D}_{\mathrm{E}j}$ is the torque disturbance affecting the electrodes around the j-th TM cage;
- $\mathrm{J}_{\mathrm{m}j}$ is the moment of inertia matrix for the j-th TM.

2.5. Test mass position

Concerning the SC position, we highlight that it is not directly controlled. Indeed, it is controlled by acting on the relative spacecraft-test mass position $\boldsymbol{r}_{\mathrm{mj\ oj}}$. This position is actuated by the GRS electrodes only along the y and z axes of the optical reference frame. Along the drag-free direction (x–axis) it is the SC itself that follows the TM by using the MPS. This is done in order to reduce the actuation noise that affects the TM along that sensitive direction.

The relative position between the TM and the spacecraft can be obtained by the inertial position $\boldsymbol{r}_{\mathrm{mj\ I}}$ expressed as the sum of different offsets, as shown in Fig. 2:

$$\boldsymbol{r}_{\mathrm{m_{jI}}} = \mathrm{T}^{\mathrm{I}}_{\mathrm{o}_j}\boldsymbol{r}_{\mathrm{m_{j\mathrm{o}_j}}} + \mathrm{T}^{\mathrm{I}}_{\mathrm{o}_j}\boldsymbol{b}_{\mathrm{m}} + \mathrm{T}^{\mathrm{I}}_{\mathrm{S}}\boldsymbol{b}_{\mathrm{S}} + \boldsymbol{r}_{\mathrm{SI}}, \tag{15}$$

$$r_{\mathrm{m_{j\mathrm{o}_j}}} = \mathrm{T}^{\mathrm{o}_j}_{\mathrm{I}} r_{\mathrm{m_{jI}}} - b_{\mathrm{m}} - \mathrm{T}^{\mathrm{o}_j}_{\mathrm{S}} b_{\mathrm{S}} - \mathrm{T}^{\mathrm{o}_j}_{\mathrm{I}} r_{\mathrm{SI}}, \tag{16}$$

where:

- $\boldsymbol{b}_{\mathrm{m}}$ is the position of the cage center with respect to the pivot point of the OA, in ORF coordinates;
- $\boldsymbol{b}_{\mathrm{S}}$ is the position of the OA pivot point with respect to the spacecraft's CoM;
- $\boldsymbol{r}_{\mathrm{SI}}$ is the inertial position of the spacecraft in the heliocentric inertial reference frame.

The final equations are

$$\ddot{\boldsymbol{r}}_{\mathrm{m_{j\mathrm{o}_j}}} = \boldsymbol{F}_{\mathrm{m}_j} - \boldsymbol{\Omega}\left(\boldsymbol{\omega}_{\mathrm{o_{jI}}}\right)\boldsymbol{b}_{\mathrm{m}} - \mathrm{T}_{\mathrm{S}}\boldsymbol{\Omega}(\boldsymbol{\omega}_{\mathrm{SI}})\boldsymbol{b}_{\mathrm{S}} - 2\boldsymbol{\omega}_{\mathrm{o_{jI}}} \times \dot{\boldsymbol{r}}_{\mathrm{m_{j\mathrm{o}_j}}} - \boldsymbol{\Omega}\left(\boldsymbol{\omega}_{\mathrm{o_{jI}}}\right)\boldsymbol{r}_{\mathrm{m_{j\mathrm{o}_j}}}, \tag{17}$$

$$F_{\mathrm{m}_j} = \mathrm{T}^{\mathrm{o}_j}_{\mathrm{I}}\mathrm{k_g}\Delta r_{\mathrm{SI}} + \frac{1}{\mathrm{m_m}}\left(F_{\mathrm{E}_j} + d_{\mathrm{E}_j}\right) - \frac{1}{\mathrm{m_S}}\mathrm{T}^{\mathrm{o}_j}_{\mathrm{S}}\left(F_{\mathrm{T}} + d_{\mathrm{\odot press}} + F_{\mathrm{met}}\right) + \frac{1}{\mathrm{m_S}}\sum_{i=1,2}\mathrm{T}^{\mathrm{o}_j}_{\mathrm{o}_i}\left(F_{\mathrm{E}_i} + d_{\mathrm{E}_i}\right), \tag{18}$$

$$\Omega(\omega) = \dot{\omega}^{\times} + \omega^{\times}\,\omega^{\times}, \tag{19}$$

$$\boldsymbol{\omega}_{\mathrm{o_{jI}}} = \mathrm{T}^{\mathrm{o}_j}_{\mathrm{S}}\boldsymbol{\omega}_{\mathrm{SI}} + \omega_{\mathrm{o_{jS}}}, \tag{20}$$

$$\omega_{\mathrm{o_{jS}}} = \dot{\xi}_j, \tag{21}$$

$$\mathrm{T}^{\mathrm{o}_j}_{\mathrm{I}} = \mathrm{T}^{\mathrm{o}_j}_{\mathrm{S}}\mathrm{T}^{\mathrm{S}}_{\mathrm{I}}, \tag{22}$$

$$\mathrm{T}^{\mathrm{o}_2}_{\mathrm{o}_1} = \mathrm{T}^{\mathrm{o}_1\top}_{\mathrm{o}_2} = \mathrm{T}^{\mathrm{o}_2}_{\mathrm{S}}\mathrm{T}^{\mathrm{o}_1\top}_{\mathrm{S}}, \tag{23}$$

$$\mathrm{T}^{\mathrm{o}_1}_{\mathrm{o}_2} = \mathrm{T}^{\mathrm{o}_2\top}_{\mathrm{o}_1} = \mathrm{T}^{\mathrm{o}_1}_{\mathrm{S}}\mathrm{T}^{\mathrm{o}_2\top}_{\mathrm{S}}, \tag{24}$$

where:

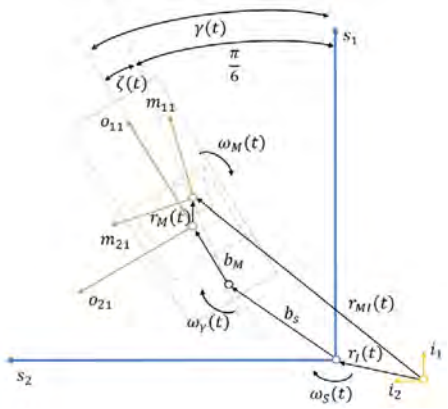

Fig. 2. TM1 vector schema.

- $\boldsymbol{r}_{\mathrm{mj\ oj}}$ is the position of the j-th TM relative to the j-th cage center;
- $\boldsymbol{b}_{\mathrm{m}}$ is the distance between the pivot of the OA and the cage center, see Fig. 2;
- $\boldsymbol{b}_{\mathrm{S}}$ is the distance between the SRF center and the pivot of the OA, see Fig. 2;
- $\boldsymbol{F}_{\mathrm{E}j}$ is the force applied by the electrodes on the j-th TM;
- $\boldsymbol{d}_{\mathrm{E}j}$ is the disturbance affecting the electrodes in the j-th cage;
- m_m is the mass of the TM;
- $\mathbf{d}_{\odot\mathrm{press}}$ and $\mathbf{F}_{\mathrm{met}}$ are the solar radiation pressure force and the meteorite impact force, respectively;
- $\Omega(\boldsymbol{\omega})$ collects the terms corresponding to the Euler and centrifugal fictitious forces that arise due to various rotating reference frames. The $\boldsymbol{\omega}^{\times}$ notation is the skew-symmetric matrix obtained from the vector $\boldsymbol{\omega}$, that represents the cross product operation;
- $\mathrm{k_g}\,\Delta\boldsymbol{r}_{\mathrm{SI}}$ represents the TM-SC gravity gradient, see Ref. [7].

2.6. Navigation mathematical model

In the development of the recovery strategies, that are presented in detail in Section 3, two different type of observers are employed. The mathematical models of both of them are presented in the following subsections.

2.6.1. Filtered differentiator model

This type of differentiator is a discrete time linear system, defined by the following Z transform transfer function:

$$F\,(z) = \frac{N\,(z-1)}{z - 1 + N\,\tau}. \tag{25}$$

The τ parameter is simply the time interval of the filter. The N parameter determines the speed of convergence to the numerical derivative. The filter has a pole at $1-N\,\tau$, therefore, the closer N is to the filter frequency $1/\tau$, the faster is the response to change in the input.

In the architecture proposed here, this filter is used to estimate the angular error velocity of the SC attitude $\boldsymbol{\omega}_{\mathrm{SC}}$ from $\mathbf{q}_{\mathrm{SC}}$, measured by the SC–SC DWS and constellation acquisition sensor (CAS). The main equations are

$$\dot{\widehat{\mathbf{q}}}_{\mathrm{sc}}(k) = \mathrm{N}\,(\mathbf{q}_{\mathrm{SC}}(k) - \mathbf{q}_{\mathrm{SC}}(k-1)\,) + (1 - N\,\tau\,)\dot{\widehat{\mathbf{q}}}_{\mathrm{sc}}(k-1), \tag{26}$$

$$\widehat{\boldsymbol{\omega}}_{\mathrm{SC}} = 2\,\mathbf{q}^{*}_{\mathrm{SC}} \otimes \dot{\widehat{\mathbf{q}}}_{\mathrm{sc}} \tag{27}$$

where $\dot{\widehat{\mathbf{q}}}_{\mathrm{sc}}$ is the estimated error quaternion derivative and $\widehat{\boldsymbol{\omega}}_{\mathrm{SC}}$ is the estimated angular error velocity. Equation (27) is the inverse quaternion kinematics relation.

Furthermore, this filter is used also to estimate the velocities of the two TMs $\boldsymbol{v}_{\mathrm{m1}}$ and $\boldsymbol{v}_{\mathrm{m2}}$ with respect to their respective optical reference frames. The filter takes as input the positions measured by the SC–TM DWS, the interferometer and the GRS. The outputs are the estimates $\widehat{\boldsymbol{v}}_{\mathrm{m_1}}$ and $\widehat{\boldsymbol{v}}_{\mathrm{m_2}}$, according to the following equation:

$$\widehat{\boldsymbol{v}}_{\mathrm{m}_j}(\mathrm{k}) = \mathrm{N}\left(\boldsymbol{r}_{\mathrm{m}_j}(\mathrm{k}) - \boldsymbol{r}_{\mathrm{m}_j}(\mathrm{k}-1)\right) + (1 - \mathrm{N}\,\tau\,)\,\widehat{\boldsymbol{v}}_{\mathrm{m}_j}(\mathrm{k}-1), \mathrm{j} = 1, 2. \tag{28}$$

2.6.2. Sliding mode observer

Observer-based methods have been also investigated as noise filtering techniques. In particular, the ability to generate a sliding motion between the measured plant output and the output of the observer ensures that a sliding mode observer produces a set of state estimates that are precisely commensurate with the actual output of the plant [35, 36].

After investigating linear observer strategies, effective solutions have been achieved considering an observer based on a super-twisting algorithm (see, e.g. Refs. [37–39]), where the discontinuous term of the driving equation is modified proportionally to the estimation error. Finally, the sliding mode observer has been designed as

$$\begin{cases} \dot{\widehat{\boldsymbol{\eta}}}_1 = \widehat{\boldsymbol{\eta}}_2 - \boldsymbol{k}_1 |\boldsymbol{e}_1|^{0.5} \boldsymbol{sign}(\boldsymbol{e}_1) & \dot{\widehat{\boldsymbol{\eta}}}_2 = \widehat{\boldsymbol{f}} - \boldsymbol{k}_2 \boldsymbol{sign}(\boldsymbol{e}_1) \end{cases} \tag{29}$$

where $e_1 \in \mathrm{R}^3$ is the observer output error, defined as

$$\boldsymbol{e_1} = \widehat{\boldsymbol{\eta}_1} - \widetilde{\boldsymbol{\theta}}_S, \tag{30}$$

$\widetilde{\theta_S} \in \mathrm{R}^3$ is the measured value of the spacecraft attitude expressed in the constellation reference frame, and $\hat{f}$ is the estimation of the spacecraft attitude dynamics, and defined as

$$\widehat{\boldsymbol{f}} = \boldsymbol{J}^{-1}[\boldsymbol{M_T} - \widehat{\boldsymbol{\eta}_2} \times \boldsymbol{J}\widehat{\boldsymbol{\eta}_2}], \tag{31}$$

where $J \in \mathrm{R}^{3\times3}$ is the matrix of inertia of the spacecraft, $M_T \in \mathrm{R}^3$ is the command torque of the attitude controller, and $\widehat{\boldsymbol{\eta}_2} \in \mathrm{R}^3$ is the estimated angular velocity of the spacecraft expressed in the constellation reference frame. Thus, the observer inputs are the spacecraft attitude measured by the available sensor, and the command torque computed by the attitude controller, while its outputs are the estimated values of spacecraft attitude and angular velocity.

The tuning process of this state observer depends upon the definition of the constant parameters k_1, $k_2 \in \mathrm{R}^{3\times3}$. Both the parameters have been defined as diagonal matrices, and achieve a trade-off between estimation accuracy and noise attenuation.

3. Recovery strategies

The main goal of this work is to design and compare different impact recovery control strategies for the LISA mission. Different configurations of controllers and sensors have been tested. In detail, three different configurations are presented and analyzed. An overview of the configuration architecture employed by each recovery strategy is sketched in Table 1.

Therefore, the main issues that had to be tackled in designing the recovery GNC system are the following:

1. *Impact detection*, that is to detect when an impact occurs;
2. *Sensor management*, that is to switch the sensors in the correct operating modes and to implement some fusion in order to obtain the most precise measurement available for each signal;
3. *Controller design*, that is to design proper controllers that can fulfil the recovery tasks.

The general idea is to limit changes from the science operative mode. However, the impact effect study [16] pointed out that keeping high resolution (HR) mode may lead the TMs to impact with their cage, causing an overall mission failure. To avoid this fatality, it appears reasonable to allow changes in the instruments state, also considering some time to settle them down.

In the rest of the section, some of the controllers and modules used in different configurations are presented. A further subsection is completely dedicated to a detailed description of each proposed strategy.

Table 1
Summary of proposed strategies.

Strategy	Sensors	Observer	SC Attitude Controller	TM Position Controller	TM Attitude Controller
1	DWS, ST	SM	PD	PID	H_∞
2	DWS, CAS, ST	FD	PD	PID	H_∞
3	DWS, CAS, ST	SM	H_∞	PID	H_∞

CAS: constellation acquisition sensor, DWS: differential wavefront sensing, FD: filtered differentiator, SM: sliding mode, ST: star tracker.

3.1. Meteoroid impact detection

The impact detector module is based on monitoring some components of the spacecraft's state. Specifically, it activates the recovery signal when at least one among the Euclidean norms of the signals of interest exceed their respective thresholds.

The first considered signal is $\widehat{\omega}_{\mathrm{SC}}$, i. e, the first derivative of the spacecraft's attitude angular error $\boldsymbol{\theta}_{\mathrm{SC}}$. The laser sensors directly measure the quaternion $\mathbf{q}_{\mathrm{SC}}$ from which $\boldsymbol{\theta}_{\mathrm{SC}}$ is easily obtained, whereas $\widehat{\omega}_{\mathrm{SC}}$ obtained according to the discrete-time equation.

$$\widehat{\boldsymbol{\omega}}_{\mathrm{SC}} = \frac{1}{\tau}(\boldsymbol{\theta}_{\mathrm{SC}}(k) - \boldsymbol{\theta}_{\mathrm{SC}}(k-1)) \tag{32}$$

where k represents the discrete-time step and $\tau = 0.01$ s is the time interval of the numerical differentiator.

The other two signals considered are the positions of the two TMs with respect to the centers of their housings, $\boldsymbol{r}_{\mathrm{m1}}$ and $\boldsymbol{r}_{\mathrm{m2}}$, respectively. They are directly measured by the electrodes positioned on the walls of the housings.

The recovery signal is triggered when one of the following conditions becomes true:

- $\|\widehat{\boldsymbol{\omega}}_{SC}\|_2 > \overline{\omega}_{SC}$;
- $\|\boldsymbol{r}_{\mathrm{m_1}}\|_2 > \bar{r}_{\mathrm{m}}$;
- $\|\boldsymbol{r}_{\mathrm{m_2}}\|_2 > \bar{r}_{\mathrm{m}}$.

The thresholds $\widehat{\omega}_{SC}$ and $\bar{r}_{\mathrm{m}}$ are scalar values tuned in order to reduce the impact detection time, that is the time elapsed between the impact instant and the instant when the recovery signal is triggered, and to have zero false negatives, that correspond to cases where the impact detector should have triggered the recovery signal but has not. This tuning has been performed by simulating all the impacts in the dataset that cause significant perturbation. The tuning found drives to define the following thresholds: $\widehat{\omega}_{SC} = 3.36$ μrad/s and $\bar{r}_{\mathrm{m}} = 5.45$ μm.

In addition to the impact detection task, it also required to formulate some conditions for performing the end of recovery, i.e., the determination of when the system is near enough to the science mode working point to be ready to switch back to the drag free controllers. This is also performed by a threshold based strategy. More specifically, when the following conditions are all true at the same time, the system is switched back to science mode:

- $|2\cos^{-1}(\mathrm{q_{SC0}})| \leq \underline{\theta}_{\mathrm{SC}}$;
- $\|\widehat{\boldsymbol{\omega}}_{SC}\|_2 \leq \underline{\omega}_{\mathrm{SC}}$;
- $\|\boldsymbol{r}_{\mathrm{m1}}\|_2 \leq \underline{r}_m$;
- $\|\boldsymbol{r}_{\mathrm{m2}}\|_2 \leq \underline{r}_m$.

where $\mathrm{q_{SC0}}$ is the scalar part of the quaternion $\mathbf{q}_{\mathrm{SC}}$, representing the attitude error of the spacecraft. The thresholds $\underline{\theta}_{\mathrm{SC}}$, $\underline{\omega}_{\mathrm{SC}}$, $\underline{r}_m$ are scalar values tuned to reduce the number of oscillations between drag-free and recovery mode at the end of recovery. The output of the tuning process provides the thresholds $\underline{\theta}_{\mathrm{SC}} = 2.1$ μrad, $\underline{\omega}_{\mathrm{SC}} = 2$ μrad/s, $\underline{r}_m = 3.56$ μm.

3.2. Recovery guidance

When at least one of the two incoming laser links are lost, the system relies on the star tracker to provide measurements regarding the spacecraft's attitude. The star tracker can measure only the inertial spacecraft attitude $\mathbf{q}_{\mathrm{SI}}$. When the laser sensors are available, they provide directly the attitude error to be fed to the attitude recovery controller, whereas when the star tracker is used, a reference attitude is needed in order to internally compute the angular error. The reference spacecraft inertial attitude is slowly changing over time, due to the orbit described by the LISA constellation. In this work, the nominal reference attitude $\boldsymbol{\omega}_{CI}$ is used as guidance during the recovery maneuver.

The final reference inertial attitude $\mathbf{q}_{\text{ref}} = \mathbf{q}_{\text{CI}}$ is computed starting from the inertial attitude at the impact instant $\mathbf{q}_{\text{SI}}(t_i)$ and propagating the attitude by integrating the quaternion kinematics:

$$\begin{aligned} \boldsymbol{q}_{\text{CI}}(t) &= \boldsymbol{q}_{\text{SI}}(t_i) \otimes \frac{\mathbf{1}}{\mathbf{2}} \int_{t_i}^{t} \boldsymbol{q}_{\text{SI}}(\tau) \otimes \boldsymbol{w}_{\text{C}}(\tau)\, d\tau, \\ \boldsymbol{w}_{\text{C}} &= [\mathbf{0} \quad \boldsymbol{\omega}_{\text{C}}]^{\top} \end{aligned} \tag{33}$$

where $\otimes$ represents the quaternion product.

When an impact occurs, a common propagation of the attitude error should be considered in each spacecraft. Indeed, it is assumed that all spacecraft enter recovery mode. While the one hit by the micrometeoroid needs to be stabilized, the others are forced into station keeping until the laser beams are reacquired.

3.3. Recovery controllers design

Different proportional–integral–derivative (PID) and proportional–derivative (PD) controllers are used by the proposed strategies in order to perform a fast laser link reacquisition. Specifically, a PD controller is employed in strategies 1 and 2 for the recovery of the spacecraft attitude. Also, the same set of PID controllers is used in every strategy for the control of the position of both test masses.

3.3.1. Spacecraft attitude PD controller

The spacecraft attitude is controlled by a simple PD control law:

$$\begin{aligned} \boldsymbol{M}_{\text{T}} &= -\boldsymbol{J}_{\text{S}}\widetilde{\boldsymbol{\omega}} - \boldsymbol{J}_{\text{S}}\widetilde{\boldsymbol{q}}, \\ \widetilde{\boldsymbol{\omega}} &= \widehat{\boldsymbol{\omega}_{\text{SI}}} - \boldsymbol{\omega}_{\text{C}}, \\ \widetilde{\boldsymbol{q}} &= \boldsymbol{q}_{\text{CI}}^{*} \otimes \widehat{\boldsymbol{q}_{\text{SI}}} \end{aligned} \tag{34}$$

$$\mathbf{J}_{\text{S}} = \begin{bmatrix} \mathbf{800} & \mathbf{0} & \mathbf{0} \\ \mathbf{0} & \mathbf{800} & \mathbf{0} \\ \mathbf{0} & \mathbf{0} & \mathbf{1000} \end{bmatrix} \tag{35}$$

where $\boldsymbol{M}_{\text{T}}$ is the torque from the thrusters, $\widetilde{\boldsymbol{\omega}}$ is the error from the desired angular velocity $\boldsymbol{\omega}_{\text{CI}}$ and $\widetilde{\boldsymbol{q}}$ is the vector part of the quaternion attitude error of the spacecraft with respect to the desired attitude $\mathbf{q}_{\text{CI}}$.

The tuning has been performed by starting with proportional and derivative weighting matrices equal to an approximate diagonal moment of inertia matrix of the spacecraft J_{S} and then further fine-tuned on the strongest impacts available in the dataset provided by ESA.

A problem that could arise from using only the vectorial part $\widetilde{\boldsymbol{q}}$ of the attitude error quaternion is the *quaternion unwinding* phenomenon. This problem arises from the fact that quaternions provide a double coverage of the orthogonal 3 by 3 matrix group SO(3), that is used to represent rotations. When using only the vector part of quaternions in a closed feedback PID control configuration, there are usually two equilibrium points $\widetilde{q} = [1 \ 0 \ 0 \ 0]^{\top}$ and $\widetilde{q} = [-1 \ 0 \ 0 \ 0]^{\top}$, of which the latter represents an undesired rotation. A common heuristic way to prevent this issue is obtained by multiplying the vectorial part by the scalar part, obtaining the following control law:

$$\boldsymbol{M}_{\text{T}} = -\,\text{J}_{\text{S}}\,\widetilde{\boldsymbol{\omega}} - \text{J}_{\text{S}}\,\widetilde{\text{q}}_0\,\widetilde{\boldsymbol{q}}. \tag{36}$$

3.3.2. TM position controller

The design for the TM position controller starts directly from a PID control law that proved to be effective for the spacecraft's attitude control problem.

The actuators that affect the quantities $\boldsymbol{r}_{\text{mj}}$ are the two GRS and the linear force of the MPS, thus a total of three different 3–dimensional PID controllers are needed.

Actually, the linear momentum transferred to the spacecraft during the impact causes the spacecraft to accelerate, that in turn generates another apparent acceleration on the relative positions between the TMs and the SC itself. For this reason the controllers that handle the linear force of the MPS thrusters compensate the average TM position $r_m^{+} = 1/2(r_{m1} + r_{m2})$ by moving the SC itself. Whereas, the controllers that handle the two GRS compensate the differential TM position $r_m^{-} = 1/2(r_{m1} - r_{m2})$, by actuating the TMs directly.

The PID controllers used are all discrete–time in parallel form, with filtered differentiation.

The Z transfer function is

$$C(z) = \text{P} + \text{I}\,\tau\frac{1}{z-1} + \text{D}\,N\frac{z-1}{z-1+N\,\tau}$$

where τ is the time interval of the controller, $\tau = 0.1$ s for the MPS controllers and $\tau = 0.01$ s for the GRS controllers.

In order to tune all the PID controllers, the Simulink PID Tuner was employed on the linearized plant. The settings used were maximum response speed and robustness. The parameters found are the following:

- For the MPS force controllers: $P = [225 \quad 225 \quad 195]^{\top}$, $I = [3 \quad 3 \quad 2.5]^{\top}$, $D = [3847 \quad 3847 \quad 3330]^{\top}$.
- For the GRS1 force controllers: $P = [-200 \quad -200 \quad -200]^{\top}$, $I = [-2 \quad -2 \quad -2]^{\top}$, $D = [-3500 \quad -3500 \quad -3500]^{\top}$.
- For the GRS2 force controllers: $P = [200 \quad 200 \quad 200]^{\top}$, $I = [2 \quad 2 \quad 2]^{\top}$, $D = [3500 \quad 3500 \quad 3500]^{\top}$.

3.4. TM recovery strategy

All the proposed recovery systems follow the same strategy as regards the TM recovery (see, Fig. 3).

The recovery system will perform a measurement fusion for both the attitude $\boldsymbol{\theta}_{\text{mj}}$ and position $\boldsymbol{r}_{\text{mj}}$ of the TMs, that is, when possible, the measurement from the local spacecraft to test mass laser sensors will replace the corresponding components of the measurements from the GRS, making it more accurate. When an impact occurs, such that it causes the activation of the TM position recovery, the GRS/laser fusion will be turned off, leaving just the GRS sensor to provide all the measurements. When the recovery is concluded the fusion will be activated again.

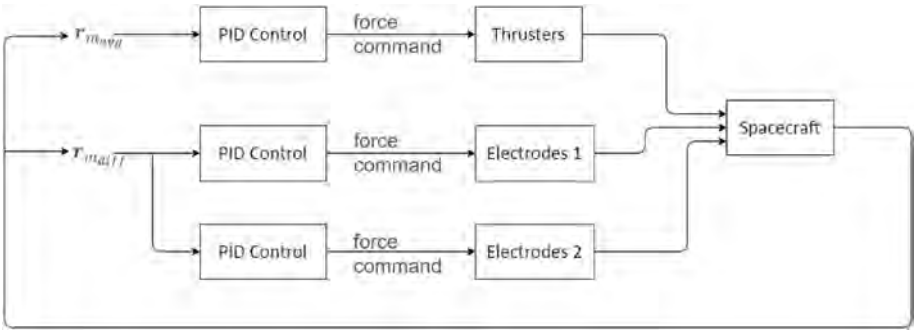

Fig. 3. Test mass position recovery controller.

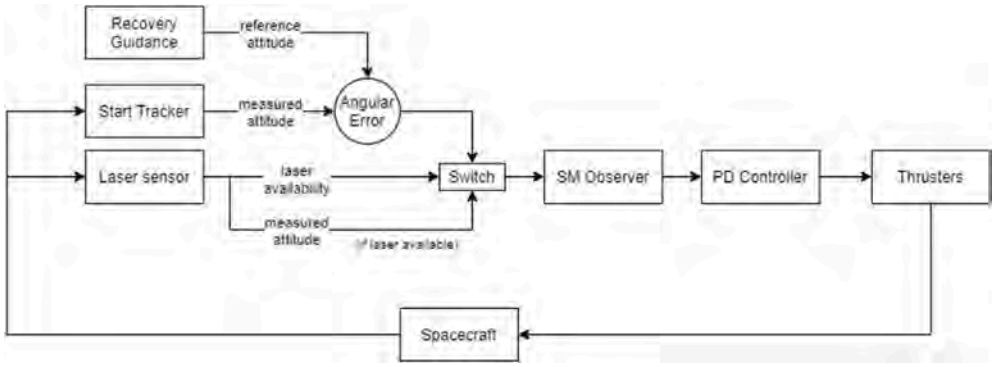

Fig. 4. Strategy 1 general architecture of the recovery controllers.

3.4.1. Strategy 1

This strategy is based on the PID/PD controllers developed in Section 3.3:

- Spacecraft attitude recovery: PD controller (Section 3.3.1).
- TM position recovery: PID controllers (Section 3.3.2).
- TM attitude recovery: H_∞ controllers of the drag free attitude control system (DFACS).

The general architecture of the spacecraft attitude recovery control system is shown in Fig. 4. Strategy 1 considers a more challenging scenario, where the CAS sensor is not available, and the only measurement available to recover the DWS is provided by the star tracker. Thus, to design an effective strategy to stabilize the system despite the high noise introduced by the star tracker, when the laser links are restored the attitude error measured through the DWS is initially expressed referred to the ORF. In this way, the spacecraft and OAs collaborate together to stabilize the spacecraft in the ORF. Finally, after a short delay $\Delta t = 10$ s, the reference frame is switched back to the CRF to restore the initial conditions.

Concerning the spacecraft attitude error $\mathbf{q}_{\mathrm{SC}}$, the controller will simply use the most accurate measurement available at each time:

1. When the DWS is available (all the azimuth and elevation angles of the incoming laser beams are smaller than 2 μrad), its measurement is used. The DWS measurement is also employed as input for the sliding mode observer to estimate the spacecraft angular ve-locity, used in combination with the attitude error for the meteoroid impact detection, as explained in Section 3.1;
2. When the DWS is lost (at least one of the azimuth and elevation angles of the incoming laser beams are greater than 2 μrad), only the star tracker is employed. The angular error computed in reference to the recovery guidance works as input for the sliding mode ob-server that provides the inputs for the recovery controller, in terms of attitude error and angular velocity.

Table 2
Strategy 1 signals sources summary.

LISA Mode	Signal	Source
Science (drag-free)	$\mathbf{q}_{\mathrm{SC}}$	(all angles* $<$ 2 μrad) SC–SC DWS
	$\boldsymbol{r}_{\mathrm{m1}}, \boldsymbol{r}_{\mathrm{m2}}$	GRS (HR) + IFO
	$\boldsymbol{\theta}_{\mathrm{m1}}, \boldsymbol{\theta}_{\mathrm{m2}}$	SC–TM DWS
	$\boldsymbol{\omega}_{\mathrm{SC}}$	SMO
Recovery	$\mathbf{q}_{\mathrm{SC}}$	(all angles* $<$ 2 μrad) SC–SC DWS (some angles* $>$ 2 μrad) SMO
	$\boldsymbol{r}_{\mathrm{m1}}, \boldsymbol{r}_{\mathrm{m2}}$	GRS (WR)
	$\boldsymbol{\theta}_{\mathrm{m1}}, \boldsymbol{\theta}_{\mathrm{m2}}$	GRS (WR)
	$\boldsymbol{\omega}_{\mathrm{SC}}$	SMO

*: angles refer to azimuth and elevation of the incoming laser beams.
SC–SC DWS: spacecraft-to-spacecraft DWS, SC–TM DWS: spacecraft-to-test mass DWS sensor, WR: wide-range mode, HR: high resolution mode, SMO: sliding mode observer.
IFO: laser interferometry (x test mass position), ST: star tracker.

Table 2 summarizes the different scenarios. For this strategy, the sliding mode observer (SMO) is employed as estimation technique both during the science and recovery mode, providing the estimation of ω_{SC} employed for the impact detection and in the recovery controller. Moreover, the SMO has been designed as noise attenuation technique, and reaching a trade off between the estimation accuracy of θ_{SC} and ω_{SC}, and noise filtering, it is able to provide to the controller the right input to stabilize the system, also under highly noisy measurements.

3.4.2. Strategy 2

This strategy is based on the PID/PD controllers developed in Section 3.3:

- Spacecraft attitude recovery: PD controller (Section 3.3.1).
- TM position recovery: PID controllers (Section 3.3.2).
- TM attitude recovery: H_∞ controllers of the DFACS.

The general architecture of the spacecraft attitude recovery control system is shown in Fig. 5.

In order to manage the loss of the laser links the strategy is to feed the spacecraft attitude recovery controllers with different attitude error ($\mathbf{q}_{\mathrm{SC}}$) signals depending on the availability of the sensors. The controller simply uses the most accurate measurement available at each time:

1. When both the DWS and CAS are available (all the azimuth and elevation angles of the incoming laser beams are smaller than 2 μrad), the CAS measurement is discarded;
2. When the DWS is lost, but not the CAS (at least one of the angles exceeds 2 μrad, but all angles are below 250 μrad), just the latter sensor is used;
3. When both sensors are lost (all the azimuth and elevation angles of the incoming laser beams are greater than 250 μrad), only the star tracker is employed, that provides the spacecraft's inertial attitude $\mathbf{q}_{\mathrm{SI}}$ and from this signal the attitude error $\mathbf{q}_{\mathrm{SC}}$ is computed as a quaternion error between the reference provided by the guidance and the measurement of the star tracker.

A filtered numerical differentiation is used to obtain the spacecraft's angular velocity for the strategy 2. Table 3 summarizes the different scenarios.

3.4.3. Strategy 3

This strategy is based on the use of the SMO in combination with the DFAC H_∞ controller, and the PID controllers developed in Section 3.3:

- Spacecraft attitude recovery: H_∞ controller.

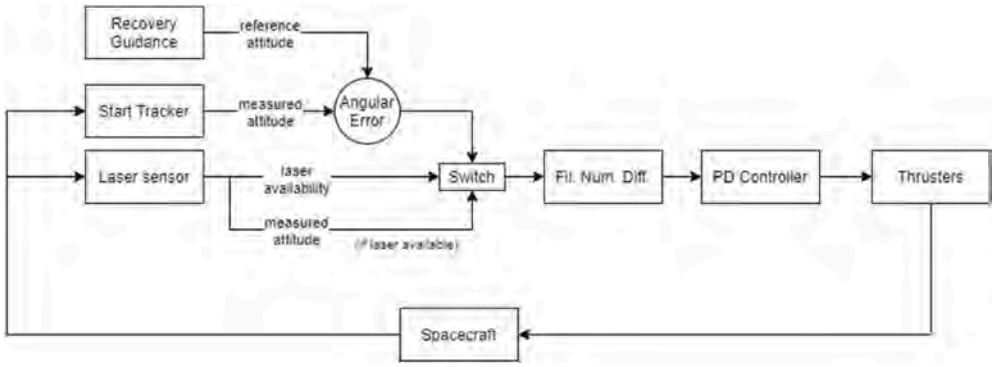

Fig. 5. Strategy 2 general architecture of the recovery controllers.

Table 3
Strategy 2 signals sources summary.

LISA Mode	Signal	Source
Science (drag-free)	$\mathbf{q}_{SC}$	(all angles* < 2 μrad) SC–SC DWS
	$\boldsymbol{r}_{m1}, \boldsymbol{r}_{m2}$	GRS (HR) + IFO
	$\boldsymbol{\theta}_{m}, \boldsymbol{\theta}_{m2}$	SC–TM DWS
	$\boldsymbol{\omega}_{SC}$	SMO
Recovery	$\mathbf{q}_{SC}$	(all angles* < 2 μrad) SC–SC DWS (some angles* > 2 μrad $\wedge$ all angles* < 250 μrad) CAS (some angles* > 250 μrad) Guidance + ST
	$\boldsymbol{r}_{m1}, \boldsymbol{r}_{m2}$	GRS (WR)
	$\boldsymbol{\theta}_{m1}, \boldsymbol{\theta}_{m2}$	GRS (WR)
	$\boldsymbol{\omega}_{SC}$	Filt. Diff. of $\mathbf{q}_{SC}$

*: angles refer to azimuth and elevation of the incoming laser beams.
SC–SC DWS: spacecraft-to-spacecraft DWS, SC–TM DWS: spacecraft-to-test mass DWS sensor, WR: wide-range mode, HR: high resolution mode.
IFO: laser interferometry (x test mass position), ST: star tracker.

- TM position recovery: PID controllers (Section 3.3.2).
- TM attitude recovery: H_∞ controllers of the DFACS.

The general architecture of the spacecraft attitude recovery control system is shown in Fig. 6. Concerning the spacecraft attitude error $\mathbf{q}_{SC}$, the controller will simply use the most accurate.

1. When both the DWS and CAS are available (all the azimuth and elevation angles of the incoming laser beams are smaller than 2 μrad), the CAS measurement is discarded;
2. When the DWS is lost, but not the CAS (at least one of the angles exceeds 2 μrad, but all angles are below 250 μrad), just the latter sensor is used. The angular error measured with the CAS works as input for the sliding mode observer that provides the inputs for the DFAC controller;
3. When both sensors are lost (all the azimuth and elevation angles of the incoming laser beams are greater than 250 μrad), only the star tracker is employed, that provides the spacecraft's inertial attitude $\mathbf{q}_{SI}$. The angular error computed in reference to the recovery guidance works as input for the sliding mode observer that provides the inputs for the DFAC controller.

Strategy 3 does not require an impact detection technique for the spacecraft attitude, since the attitude controller during the recovery mode is still the DFAC. Otherwise, for the TMs, the impact detection signal is still employed to switch correctly to the PID recovery controller, as explained in Section 3.1. Table 4 summarizes the different scenarios.

For this strategy, the SMO is employed as estimation technique during recovery mode. In particular, it has been designed to compute θ_{SC} in function of the sensor measurement and the control input u, limiting the variation of the output signal in each simulation step. In this way, losing estimation accuracy after the impact occurs, it is possible to help the DFAC controller providing an input signal within its sensitiveness, and making it able to stabilize the disturbances.

4. Simulation campaign

In this chapter, the recovery strategies proposed in the previous section are tested using the Thales Alenia Space Italy high-fidelity simulator. In detail, we propose three different approaches for testing the effectiveness of the proposed methodology. The first one is represented by a single case simulations, featuring the strongest impact - in terms of transferred angular momento to the spacecraft - of the ESA dataset. The second part is a MC campaign accounting for uncertainties on the physical features of the spacecraft. Finally, a stress test is carried out determining the range of values in which the stability of the

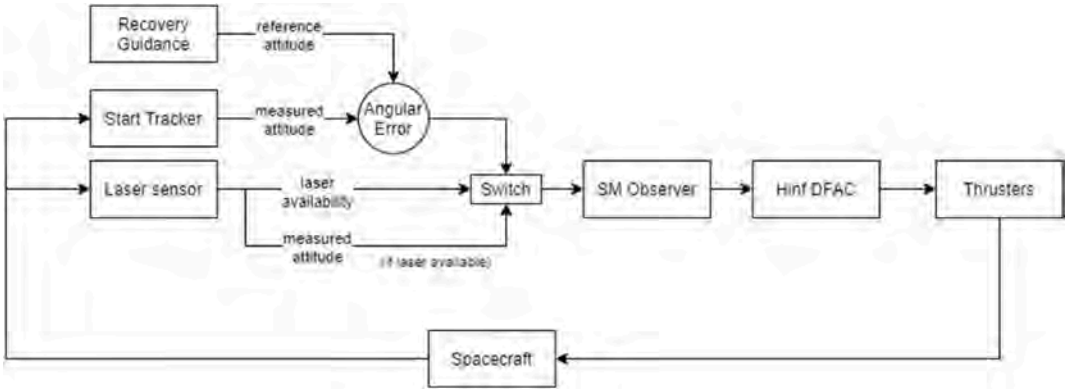

Fig. 6. Strategy 3 general architecture of the recovery controllers. Measurement available at each time.

Table 4
Strategy 3 signals sources summary.

LISA Mode	Signal	Source
Science (drag-free)	$\mathbf{q}_{SC}$	(all angles* $<$ 2 μrad) SC–SC DWS
	$\boldsymbol{r}_{m1}, \boldsymbol{r}_{m2}$	GRS (HR) + IFO
	$\boldsymbol{\theta}_{m1}, \boldsymbol{\theta}_{m2}$	SC–TM DWS
	$\boldsymbol{\omega}_{SC}$	SMO
Recovery	$\mathbf{q}_{SC}$	(all angles* $<$ 2 μrad) SC–SC DWS (some angles* $>$ 2 μrad) SMO
	$\boldsymbol{r}_{m1}, \boldsymbol{r}_{m2}$	GRS (WR)
	$\boldsymbol{\theta}_{m1}, \boldsymbol{\theta}_{m2}$	GRS (WR)
	$\boldsymbol{\omega}_{SC}$	SMO

*: angles refer to azimuth and elevation of the incoming laser beams.
SC–SC DWS: spacecraft-to-spacecraft DWS, SC–TM DWS: spacecraft-to-test mass DWS sensor, WR: wide-range mode, HR: high resolution mode, SMO: sliding mode observer.
IFO: laser interferometry (x test mass position), ST: star tracker.

spacecraft is assured by each recovery strategy.

4.1. LISA high-fidelity simulator

The study presented in this paper takes advantage of the Thales Alenia Space high-fidelity simulator [34]. The simulator was based on the new mission end-to-end simulator (NUMES) simulation environment that enables one to easily build-up specific end-to-end software environments for different missions, being based on the heritages of other ESA space missions like SAX, GOCE, and ExoMars. The NUMES suite is able to numerically simulate, with a high level of fidelity, the dynamics of one or more satellites subject to various external environmental disturbances, also including models of the sensors and actuators entering in the control loop. The validated range of C/C++, Fortran sources file and Matlab/Octave Python macros can be used on different operative systems without requiring any proprietary licences.

In particular the Thales simulator includes the following mathematical models:

- The LISA SC full dynamics, accounting for all the 20° of freedom of the constellation.
- Sensor and actuators defined by mass properties, size, field-of-views, rnges, mounting and other mechanical features.
- Environmental disturbances.
- Orbital ephemeris.
- DFACS controller.

According to the purpose of the study, the LISA simulator has been enhanced by adding further simulation blocks required to study the effects of micrometeoroid impacts. In particular an impact generator has been included within the simulation environment, as well as the logic and the control loop in charge of the recovery phase. For impact modelling, we consider a full elastic impact between spacecraft and meteoroid. The elastic impact is more conservative than considering the energy dissipation related to structural deformation. Moreover, this choice is also driven by the fact that data about spacecraft structural design are not available in the early stage of the LISA mission. Nevertheless, one has to consider that the impact with flexible surfaces (i.e. solar panels) may lead to vibrations, and may introduce significant disturbances in the spacecraft dynamics, as can be seen for a general spacecraft in Ref. [40]. However, this phenomenon has not been considered since it can be limited and managed in the spacecraft design.

Finally, the LISA DFACS model accounts also for a constellation equivalent model for SC relative position and attitude. The SC orbit takes into account the gravitational attraction of the Sun plus third-body gravitational disturbances due to Earth, Moon, Mars, Jupiter, Venus, and Saturn. A sketch of the simulator architecture is given in Fig. 7.

4.2. Single-impact simulation

The single-impact simulations consider the spacecraft perturbation related to the impact generating the highest disturbance from the impact data-set (in terms of transferred angular momentum). It is characterized by the following values of transferred linear and angular momentum:

$$p = [-2.50 \quad -0.90 \quad 14.9] \cdot 10^{-3} Ns$$
$$h = [-4.00 \quad 19.9 \quad 0.60] \cdot 10^{-3} Nms$$

and it has been considered as first step of analysis for the proposed recovery strategies.

4.2.1. Strategy 1

Strategy 1 is characterized by the absence of the CAS sensor (the star tracker is the unique available sensor for spacecraft attitude stabilization and the DWS recovery). As explained in Section 3.5, the recovery strategy is based on the PID/PD controllers and employs the SMO as the system state estimation algorithm. Moreover, use of the ORF helps the system to recover the DWS faster, achieving interesting performance. Fig. 8 shows the recovery phase behavior for the strongest impact from the ESA dataset. The main parameter considered for the strategies evaluation is the recovery time, Fig. 8e. Strategy 1 completes the recovery process in sufficiently short time, 640 s for the spacecraft attitude and 648 s for the TM position, providing acceptable overshoots in the related variables, $|\theta_{SC}| < 0.0011$ rad and $|r_{T\,M}| < 6.03 \cdot 10^{-5}\ m$.

4.2.2. Strategy 2

As explained in Section 3.6, strategy 2 is based on the PID/PD controllers and the filtered numerical differentiator for the estimation of the spacecraft angular velocity. The main objective of this strategy is to have a recovery controller that reacts rapidly, able to restore the spacecraft initial conditions in very short times without losing the CAS sensor.

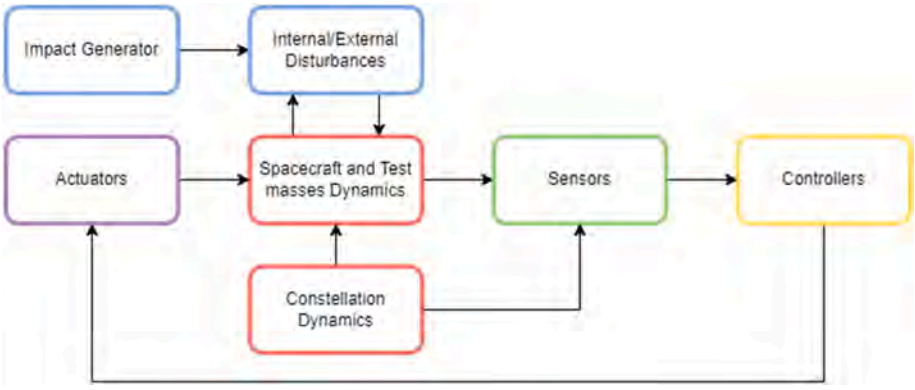

Fig. 7. Lisa simulator architecture.

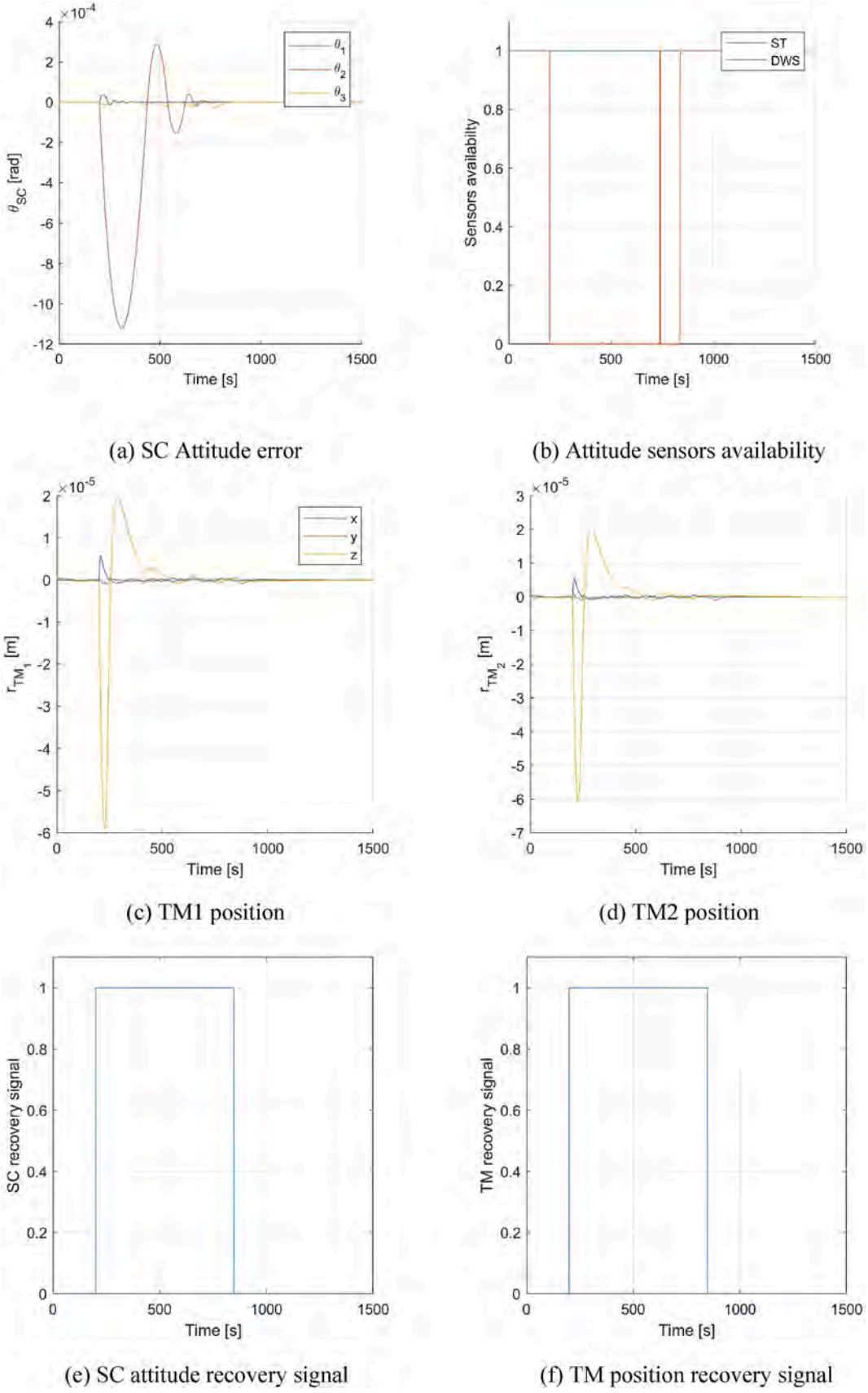

Fig. 8. Strategy 1: Recovery system simulation for strongest impact.

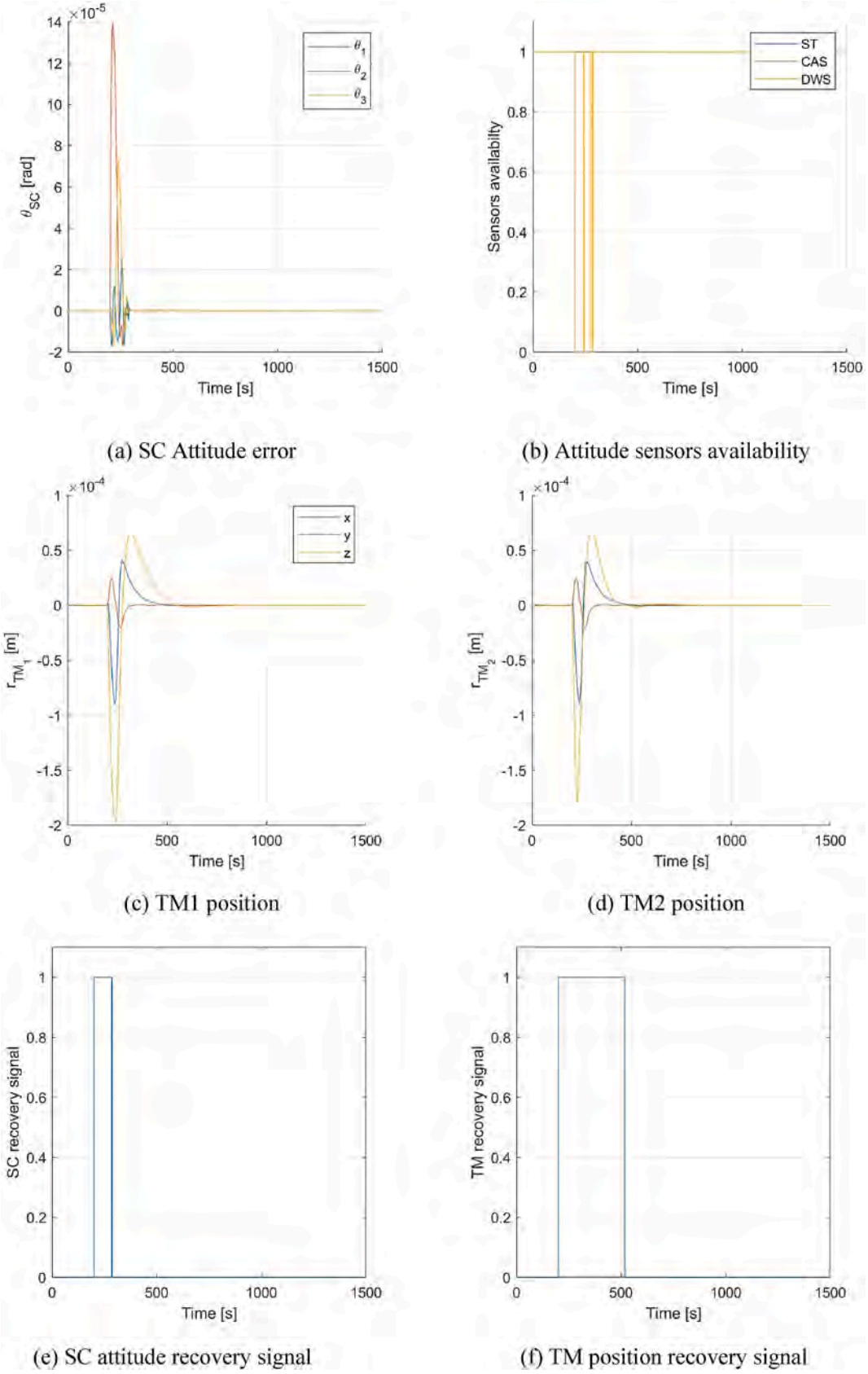

Fig. 9. Strategy 2: Recovery system simulation for strongest impact.

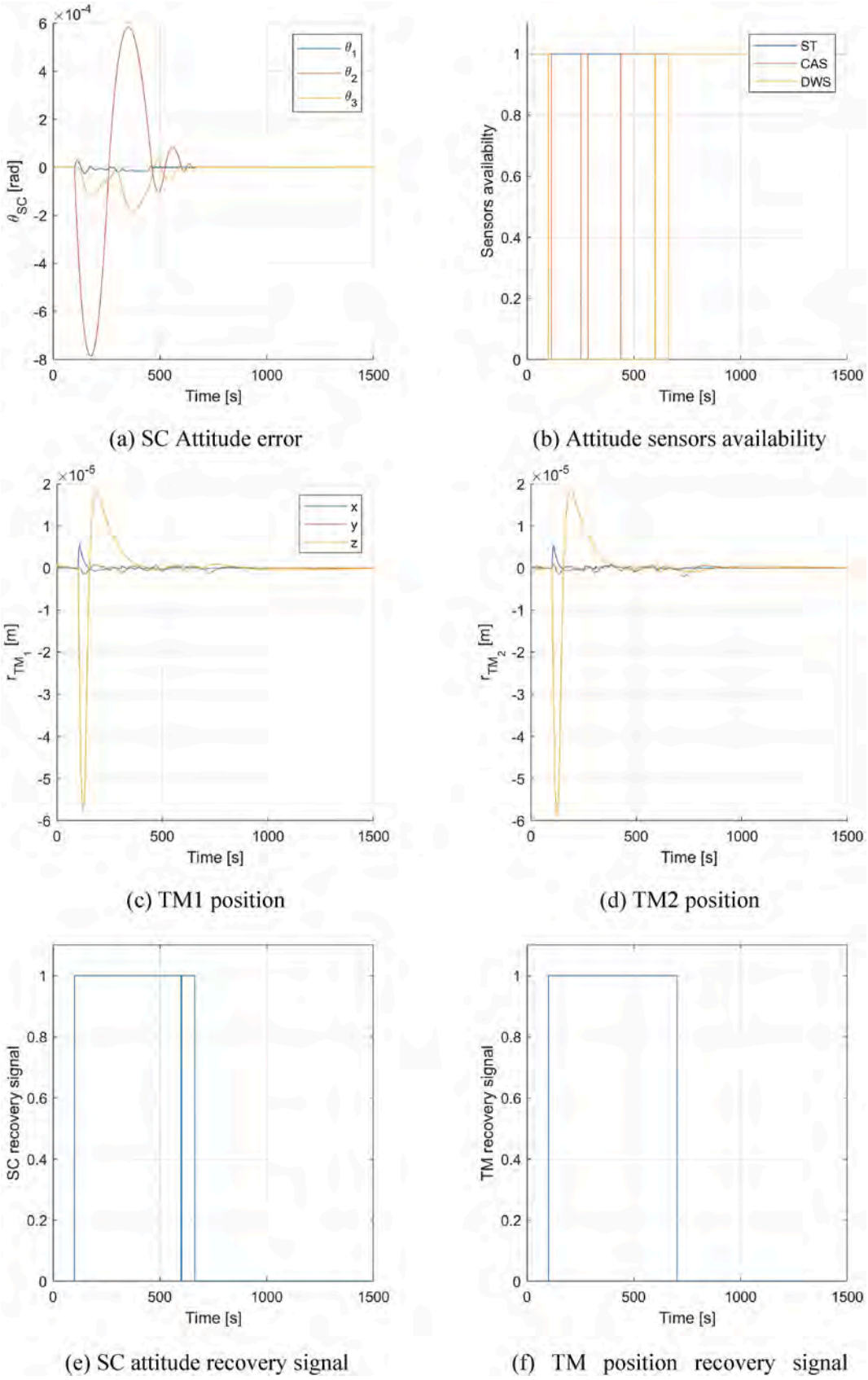

Fig. 10. Strategy 3: Recovery system simulation for strongest impact.

Table 5
Monte Carlo campaign.

Parameter	Uncertainty range
m_s	[1360, 1500]
m_M	[1.95, 1.97]
J_s	diag: [778,800],[751,800],[953,1000] non-diag: ±13
J_M	$\pm 0.3 \cdot 10^{-4}$ for all elements
${}^sT\,T$, ${}^sRR$, ${}^sRT$	$\pm 3 \cdot 10^{-6}$ for all elements
${}^sT\,R$	$\pm 3 \cdot 10^{-9}$ for all elements
p_m	±[0.001,0.004] for all elements

All the values are expressed in the International System of Units.

Fig. 9 shows the simulation results for the strongest impact from the ESA dataset. Strategy 2 completes the recovery process in notably short time, 84 s for the spacecraft attitude and 316 s for the TM position, providing restrained overshoots in the related variables, $|\theta_{SC}| < 1.38 \cdot 10^{-4}$ rad and $|r_{T\,M}| < 1.97 \cdot 10^{-4}$ m.

4.2.3. Strategy 3

As explained in Section 3.7, strategy 3 is based on the combination of the SMO with the DFAC H_∞ controller. The main objective of this strategy is avoiding the implementation of an attitude controller for the recovery mode by using the DFAC H_∞ controller, where the attitude error input is generated by the SMO. Thus, opposed to the previous strategy, there is not a recovery controller. The spacecraft attitude recovery signal is strictly related to the DWS recovery, and employed to maintain the TM recovery mode until the sensor is recovered. Fig. 10 shows the simulation results for the strongest impact from the ESA dataset. Strategy 3 completes the recovery process in relatively short time, 552 s for the spacecraft attitude and 600 s for the TM position, providing restrained overshoots in the related variables, $|\theta_{SC}| < 7.85 \cdot 10^{-4}$ rad and $|r_{T\,M}| < 5.91 \cdot 10^{-5}$ m.

All the strategies show good performance in terms of recovery time and errors overshoot. Strategy 2 has been designed to be more reactive than the others. In fact, it takes a notably short time to restore the spacecraft attitude, but, at the same time, this reactivity leads to higher disturbances in the TMs, where an higher overshoot is reported. Strategies 1 and 3 have comparable results both in terms of errors overshoot and recovery time, despite the differences in sensor availability.

4.3. Monte Carlo simulations

In this section, the results of the MC campaign considering uncertainties in the physical parameters of the spacecraft are reported. Impacts have been randomly generated considering a disturbance - in terms of transferred linear and angular momentum - of the same order of magnitude of the ESA dataset worst case. Critical parameters and their uncertainties, summarized in Table 5, have been selected and combined in a MC simulation campaign in order to fulfil the strategies analysis. In particular, 100 simulations have been carried out considering begin-of-life spacecraft mass $m_s = 1500$ kg, and 100 simulations with end-of-life spacecraft mass $m_s = 1360$ kg.

Remark 1. In the study presented here, the impact cases considered are the result of previous study and analysis conducted by ESA, consisting of 219728 different impacts whose features are sketched in [16]. The control system design is tested for many impacts to prove the control robustness against the force and momentum exchanged between the SC and micrometeoroids. Nevertheless, considering a realistic impact distribution in relationship to the impact action rate, it could be an interesting topic for future and deeper study of the LISA mission.

The obtained simulation results are reported in Figs. 11–13, respectively, for strategy 1, strategy 2 and strategy 3. Strategies 1 and 2 fulfil the desired task in each scenario, and showing satisfying robustness to parameter uncertainties and to different impact scenarios. However, Strategy 3 is still able to stabilize the spacecraft despite its sensitiveness to the disturbances, but it shows less robustness versus parameter uncertainties, especially for the stabilization around the z-axis, leading to higher overshoots and RET values. The Monte Carlo campaign results are summarized in Table 6. A summary and comparison (among the three different strategies) of SC and TM recovery times is shown in Fig. 14.

4.4. Stress test

In this section, the recovery strategies are tested considering intensive simulations, where the spacecraft is subjected to increasingly strong impacts. Finally, the results of the stress test show the limitation of the proposed recovery strategies in terms of maximum disturbances in comparison with the strongest impacts available in the ESA dataset.

The stress test consists of performing complete simulations considering increasingly strong impacts, until a divergent behaviour of some variable is observed. In this way, it is possible to define a maximum disturbance value, in terms of transferred linear and angular momentum, such that the recovery strategy assures system stability. Thus, to fully understand the capabilities of the proposed strategy, unidirectional impacts have been considered. For each direction, four different critical cases have been analyzed as worst-case scenarios.

Each impact has been modelled as an impulsive force acting for $\Delta t =$ 0.01 s, and defined only by a component of value.where $k = 1, 2, \ldots, n_c$ where n_c is an impact previous to a critical solution for the spacecraft attitude or the TMs position. Considering a force with component F_z, four different cases have been considered:

- An impact generating a disturbance force along only the z–axis.
- An impact generating a disturbance force and the highest disturbance torque around the x–axis.
- An impact generating a disturbance force and the highest disturbance torque around the y–axis.
- An impact generating a disturbance force and the highest disturbance torques around the x and y axes.

The same holds for impacts with components F_x and F_y, considering, respectively, disturbance torques around the y and z axes, and the x and z axes.

For each strategy, a maximum transferred linear momentum equal to 0.02 N is considered, and the simulation scenarios are summarized in Table 7. For each simulation case, the limit value of transferred linear momentum is marked with a circle (○) if the instability is related to the SC attitude, or a square (□) if related to TM position.

4.4.1. Strategy 1

This strategy, described in Section 3.5, is based on the PID/PD controllers developed in Section 3.3, combined with the SMO described is Section 2.6.2. Its performance is discussed in section 4, while in this section the limits of the proposed strategy are defined and compared with the ESA dataset, analyzed through the Monte Carlo simulations campaign. Fig. 15 shows all the disturbances applied to the system during the stress test, and expressed as transferred linear and angular momentum. For each simulation case, summarized in Table 7, the transferred angular and linear momentum leading to critical behaviour (attitude or TM instability) is identified.

Strategy 1 is able to assure the stability of the system if the transferred linear momentum p_x is smaller than $p_{x,lim} = 0.006$ N. For values $p_{x,lim} < |p_x| < 0.018$ N, the proposed strategy is still able to assure the system stability if the transferred angular momentum is $|h_z| < 0.015$ Nms. Disturbances with component p_y are always stabilized if the transferred linear momentum is smaller than $p_{y,lim} = 0.013$ N. Finally, disturbances with component p_z are always stabilized if the transferred angular momentum is smaller than $p_{z,lim} = 0.016$ N. For values $p_{z,lim} <$ |

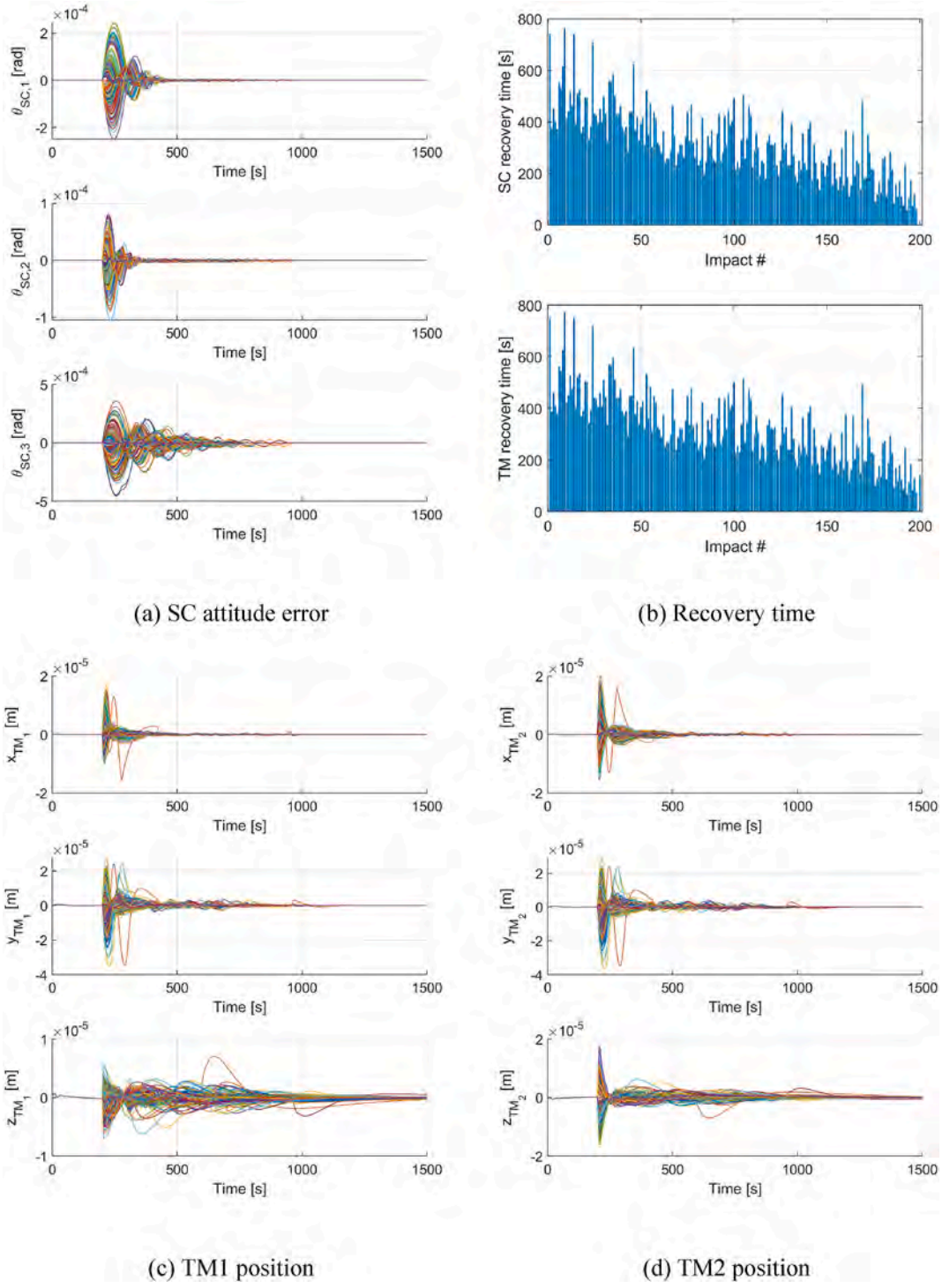

Fig. 11. Monte Carlo campaign with parameter uncertainties strategy 1.

$p_z| < 0.018$ N, the proposed strategy is still able to assure the system stability if the transferred angular momentum is $|h_x| < 0.041$ Nms. This results are summarized in Table 8.

In particular, the following considerations can be made:

- Having a disturbance that acts also on the spacecraft rotation around the y-axis does not have influence on the TM stabilization.
- Disturbance torque around the z and x axes can lead to instabilities that spacecraft recovery mode is not able to handle, also compromising the stabilization of the TMs.

4.4.2. Strategy 2

This strategy, described in Section 3.6, is based on the PID/PD controllers developed in Section 3.3. Its performance is discussed in section 4, while in this section the limits of the proposed strategy are defined and compared with the ESA dataset, analyzed through the Monte Carlo simulations campaign. Fig. 16 shows all the disturbances applied to the system during the stress test, and expressed as transferred linear and angular momentum. For each simulation case, summarized in Table 7, the transferred angular and linear momentum leading to critical behaviour (attitude or TM instability) is identified.

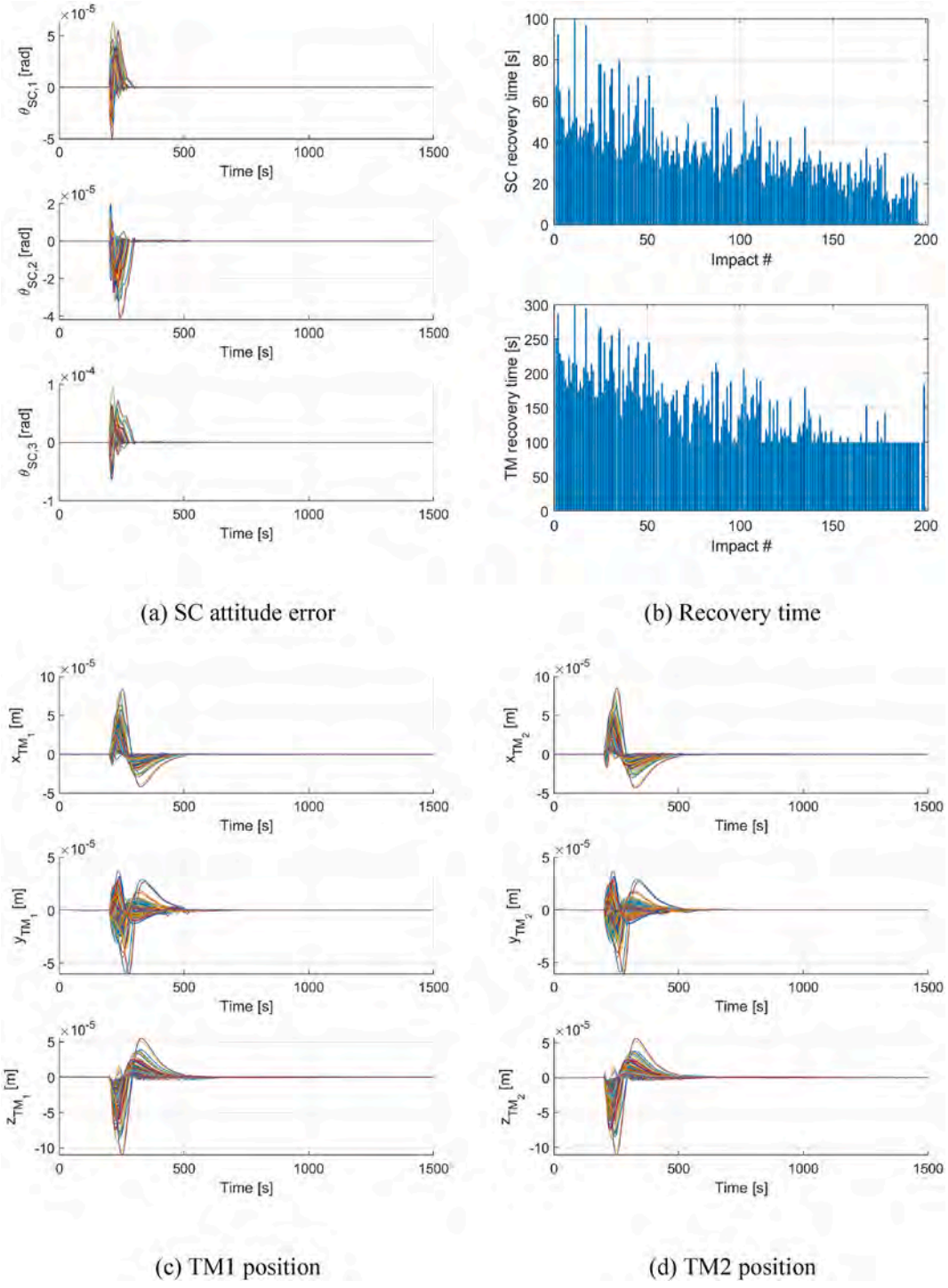

Fig. 12. Monte Carlo campaign with parameter uncertainties strategy 2.

Strategy 2 is able to assure the stability of the system if the transferred linear momentum p_x is smaller than $p_{x,lim} = 0.009$ N. For values $p_{x,lim} < |p_x| < 0.018$ N, the proposed strategy is still able to assure the system stability if the transferred angular momentum is $|h_z| < 0.018$ Nms. Disturbances with component p_y are always stabilized if the transferred linear momentum is smaller than $p_{y,lim} = 0.015$ N. For values $p_{y,lim} < |p_y| < 0.022$ N, the disturbances are stabilized if the transferred angular momentum is $|h_z| < 0.018$ Nms. Finally, disturbances with component p_z are always stabilized if the transferred angular momentum is smaller than $p_{z,lim} = 0.008$ N. For values $|p_z| > p_{z,lim}$, the proposed strategy is still able to assure the system stability if the transferred angular momentum is $|h_x| < 0.020$ Nms. This results are summarized in Table 8.

In particular, the following considerations can be made:

- Strategy 2 reactivity leads to an overall reaction of the system, thus, independently from the disturbance all the degree of freedom are involved in the system stabilization. This makes it impossible to understand exactly where the instabilities take place. Thus, as opposed to the other strategies, the critical cases are denoted with a colored triangle.

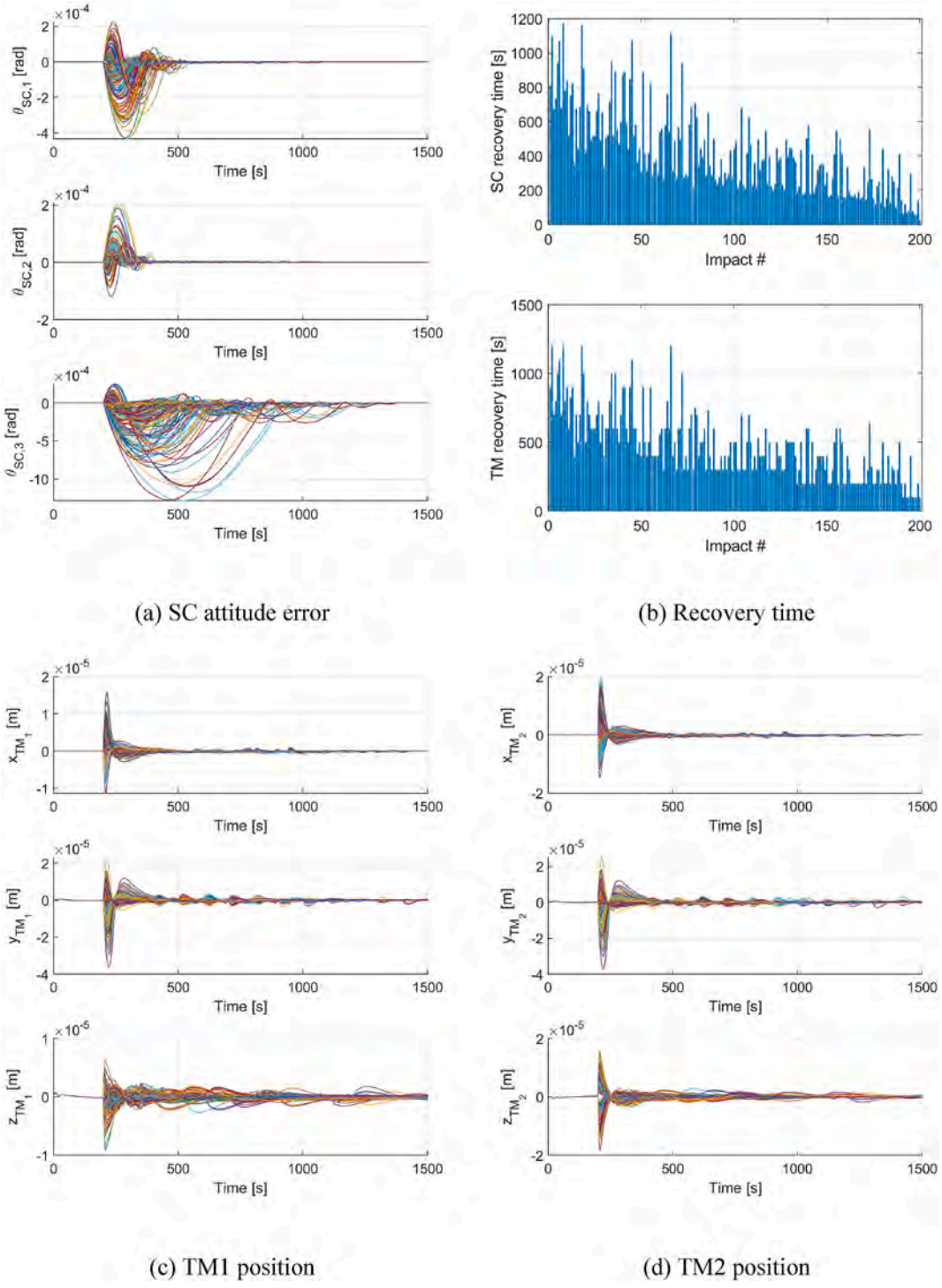

Fig. 13. Monte Carlo campaign with parameter uncertainties strategy 3.

- Having a disturbance that acts also on the spacecraft rotation around the y-axis does not have influence on the TM stabilization.
- Disturbance torque around the z and x axes can lead to instabilities that spacecraft recovery mode is not able to handle.

4.4.3. Strategy 3

This strategy is based on the use of the SMO, described in Section 2.6.2, with the DFAC H_∞ controller. Its performance is discussed in section 4, while in this section the limits of the proposed strategy are defined and compared with the ESA dataset, analyzed through the Monte Carlo simulations campaign. Fig. 17 shows all the disturbances applied to the system during the stress test, and expressed as transferred linear and angular momentum. For each simulation case, summarized in Table 7, the transferred angular and linear momentum leading to critical behaviour (attitude or TM instability) is identified.

Strategy 3 is able to assure the stability of the system if the transferred linear momentum p_x is smaller than $p_{x,lim} = 0.007$ N. For values $p_{x,lim} < |p_x| < 0.018$ N, the proposed strategy is still able to assure the system stability if the transferred angular momentum is $|h_z| < 0.018$ Nms. Disturbances with component p_y are always stabilized if the transferred linear momentum is smaller than $p_{y,lim} = 0.0012$ N. For values $p_{y,lim} < |p_y| < 0.018$ N, the disturbances are stabilized if the

Table 6
Monte Carlo.

Strategy 1				
Variable	Max	Min	Mean	STD
MAX $\theta_{S,1}$ [μrad]	248	1.48	95.1	61.1
MAX $\theta_{S,2}$ [μrad]	104	1.45	31.0	21.6
MAX $\theta_{S,3}$ [μrad]	453	0.91	122	97.5
MAX $x_{T\,M}$ [μm]	[16.7 20.0]	[0.65 0.84]	[5.33 7.91]	[3.61 4.56]
MAX $y_{T\,M}$ [μm]	[35.4 36.4]	[1.19 1.14]	[9.42 10.2]	[7.07 7.30]
MAX $z_{T\,M}$ [μm]	[7.12 17.5]	[0.80 1.23]	[2.63 7.38]	[1.32 3.91]
SC RET [s]	772	0	325	138
TM RET [s]	772	0	326	137
Strategy 2				
MAX $\theta_{S,1}$ [μrad]	62.9	1.60	21.3	10.7
MAX $\theta_{S,2}$ [μrad]	41.9	2.30	13.3	7.04
MAX $\theta_{S,3}$ [μrad]	93.1	4.36	27.1	15.7
MAX $x_{T\,M}$ [μm]	[83.7 85.2]	[2.14 1.63]	[19.8 19.8]	[15.6 15.7]
MAX $y_{T\,M}$ [μm]	[60.3 61.0]	[1.74 1.77]	[14.9 15.0]	[9.95 10.0]
MAX $z_{T\,M}$ [μm]	[110,111]	[4.76 3.59]	[28.7 28.1]	[20.2 20.2]
SC RET [s]	103	2.64	38.2	18.5
TM RET [s]	299	0	147	50.7
Strategy 3				
MAX $\theta_{S,1}$ [μrad]	432	2.91	121	94.8
MAX $\theta_{S,2}$ [μrad]	207	1.45	38.6	37.7
MAX $\theta_{S,3}$ [μrad]	1300	0.40	248	271
MAX $x_{T\,M}$ [μm]	[16.1 19.8]	[0.77 0.77]	[4.83 6.75]	[3.28 4.12]
MAX $y_{T\,M}$ [μm]	[35.8 37.1]	[1.09 0.78]	[8.16 8.91]	[6.21 6.53]
MAX $z_{T\,M}$ [μm]	[9.08 18.2]	[0.80 0.95]	[2.23 7.20]	[1.39 3.75]
SC RET [s]	1182	37.7	430	245
TM RET [s]	1200	100	478	245

transferred angular momentum is $|h_z| < 0.022$ Nms and $|h_x| < 0.07$. Finally, disturbances with component p_z are always stabilized if the transferred angular momentum is smaller than $p_{z,lim} = 0.014$ N. For values $p_{z,lim} < |p_z| < 0.019$ N, the proposed strategy is still able to assure the system stability if the transferred angular momentum is $|h_x| < 0.036$ Nms. This results are summarized in Table 8.

For strategy 3, the same consideration made for strategy 1 holds.

The stress test simulations results, shown in Figs. 15–17, are compared in Table 8. In comparison with the ESA dataset impacts, all the strategies show satisfactory bounds of operative range. In particular:

- For strategy 1, transferred linear momentum lower bounds are all higher than the values from the ESA dataset.
- For strategies 2 and 3, transferred linear momentum from the ESA dataset can exceed the lower bounds. However, the transferred angular momentum never exceeds the limits computed for the spacecraft attitude stabilization.

Table 7
Stress test scenarios.

Case	F_x	F_y	F_z
1	p_x	p_y	p_z
2	$p_x + h_y$	$p_y + h_x$	$p_z + h_x$
3	$p_x + h_z$	$p_y + h_z$	$p_z + h_y$
4	$p_x + h_y + h_z$	$p_y + h_x + h_z$	$p_z + h_x + h_y$

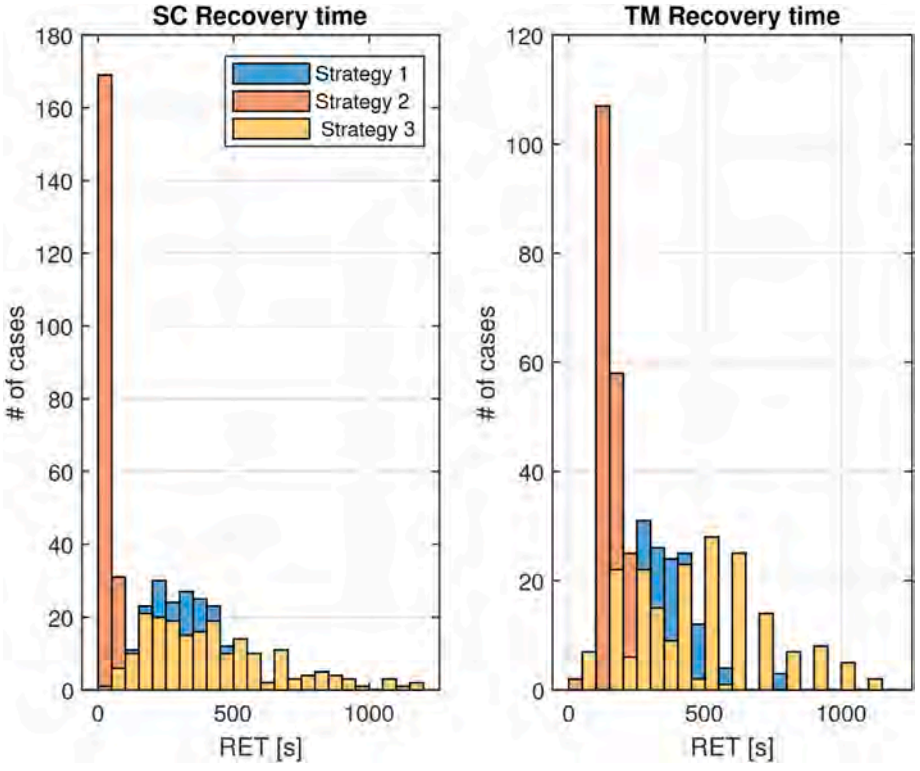

Fig. 14. Summary and comparison of recovery times.

$F = k0.1,$ (37)

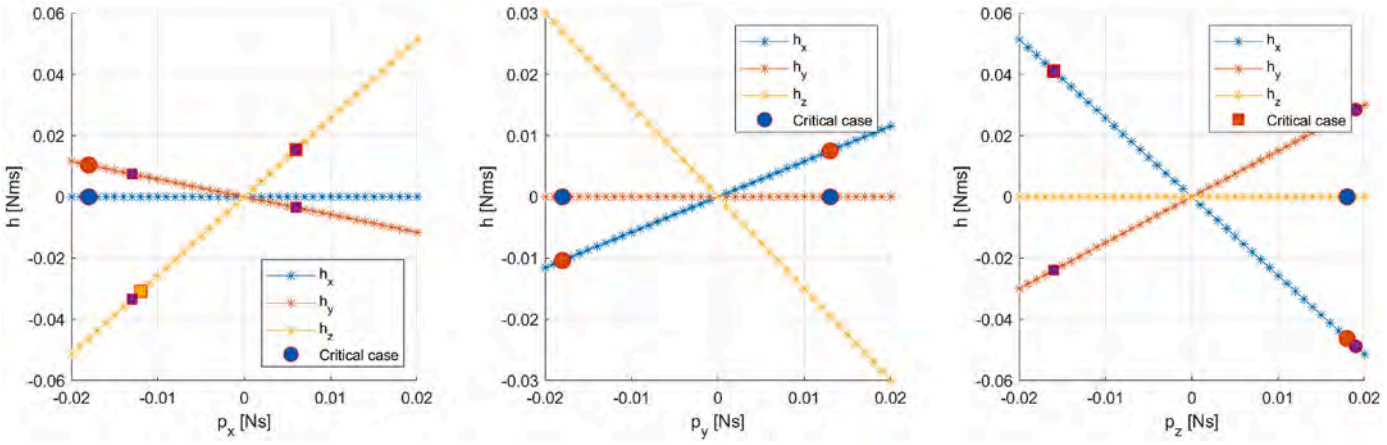

Fig. 15. Stress tests maximum disturbances for strategy 1.

Table 8
Stress test results.

Source	Linear momentum [Ns]			Angular momentum [Nms]		
	$\lvert p_x \rvert$	$\lvert p_y \rvert$	$\lvert p_z \rvert$	$\lvert h_x \rvert$	$\lvert h_y \rvert$	$\lvert h_z \rvert$
ESA dataset	0.0032	0.0057	0.0150	0.0198	0.0199	0.0047
ST S1	[0.006,0.018]	0.013	[0.016, 0.018]	0.041	>0.03	0.015
ST S2	[0.009, 0.018]	[0.015, 0.022]	[0.008, >0.02]	0.020	>0.03	0.018
ST S3	[0.007, 0.018]	[0.012, 0.018]	[0.014, 0.019]	0.036	>0.03	0.018

ST: Stress test results.

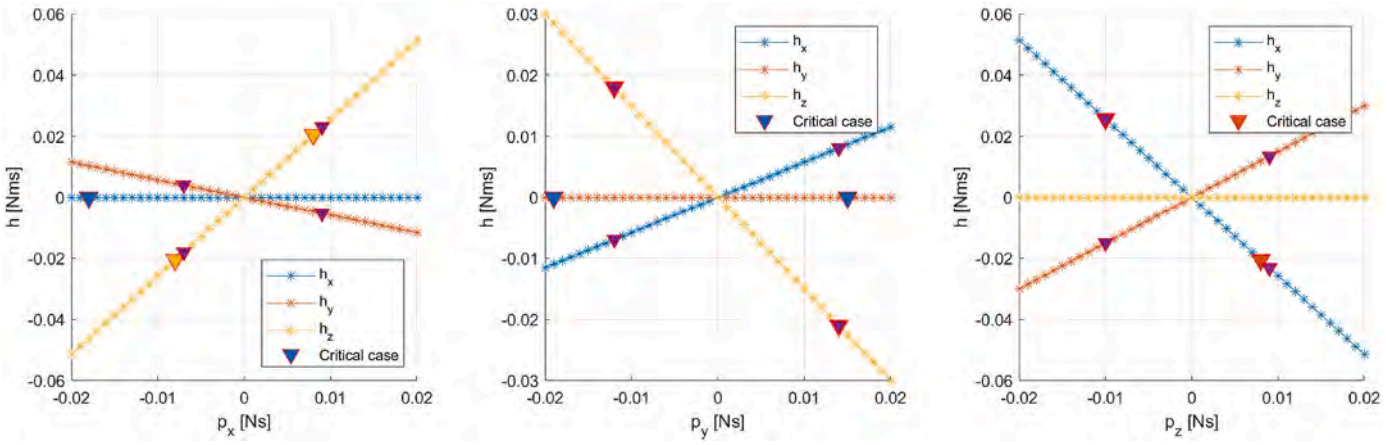

Fig. 16. Stress tests maximum disturbances for strategy 2.

In general, considering impacts with the same intensity and direction and opposite verse leads to different solutions. This effect is related to the actuators configuration that is not symmetrical.

5. Conclusion

This paper investigates different solutions to cope with micro-meteoroid impacts in the LISA mission. During the science mode, some meteoroid impacts have enough energy to generate a critical perturbation of the spacecraft attitude or position of the test masses. If laser links are lost, then the overall system becomes unstable.

In this paper, an impact detector is designed, evaluating the orientation and angular speed of the spacecraft by means of an observer. Then, the system stabilization and the laser links recovery is addressed considering three different strategies. A common solution for the test masses is adopted, designing a reactive PID controller to capture them, preventing collisions with the cage. The same strategy is adopted for attitude stabilization in comparison with a second one, adopting a sliding mode observer in combination with the H_∞ DFAC. A third solution is provided, not considering the CAS sensors, and combining the

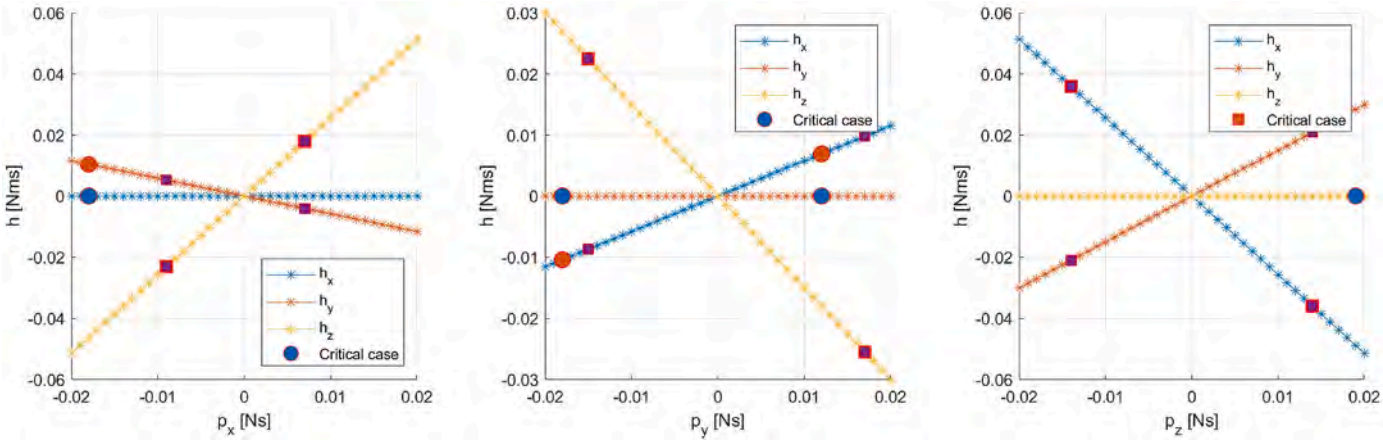

Fig. 17. Stress tests maximum disturbances for strategy 3.

PID controller with the sliding mode observer. The performance of the proposed strategies are compared by means of simulations, considering a large impact data set. A Monte Carlo simulation campaign is performed to evaluate the robustness of the strategies with respect to parameters variation. Finally, a stress test is carried out to evaluate the effective improvement given by each strategy. Each strategy is able to fulfill the desired task in a short time, with different performance. In particular, the strategies using the sliding mode observer require more time to reacquire the laser links. However, a smoother reaction to the impact stabilization is safer for the test masses, compared to a more reactive approach. The spacecraft rotation acts as a perturbation in the test masses position. Having a smoother rotation makes the test mass closed-loop system more stable, helping the controller to guarantee position requirements. In conclusion, all the considered strategies address successfully the micro-meteoroid impact phenomena, but with different characteristics. Future studies may address a realistic impact distribution in relation to impacts action rate. It may be an interesting investigation for further and deeper understanding of closed-loop system performance of the LISA mission.

Declaration of competing interest

The authors declare the following financial interests/personal relationships which may be considered as potential competing interests: Carlo Novara reports financial support was provided by European Space Agency.

Appendix A. Reference systems

The general configuration of all the reference systems, or reference frames, is depicted in Fig. 18. The following frames are defined:

- *Inertial reference frame* (IRF): a quasi-inertial frame, that can be assumed inertial for this application, with its origin in the Sun. The $\mathbf{I}_3$ unit vector is directed perpendicular to Earth's orbital plane around the Sun, $\mathbf{I}_1$ is directed along the line that connects the Sun to Earth at the Vernal Equinox and $\mathbf{I}_2$ is obtained by the right-hand rule. IRF is defined by the set $\{O_I, \mathbf{I}_1, \mathbf{I}_2, \mathbf{I}_3\}$ and represented with the letter I.
- *Constellation reference frame* (CRF): a reference frame that is reconstructed onboard and allows the spacecraft to evaluate its attitude with respect to the constellation formation. The origin is at the spacecraft's center, $\mathbf{c}_3$ is perpendicular to the plane defined by the two non-parallel incoming laser beams, $\mathbf{c}_1$ lies on the same plane and is defined as the bisectrix of the angle formed by the two incoming laser beams. CRF is defined by the set $\{O_C, \mathbf{c}_1, \mathbf{c}_2, \mathbf{c}_3\}$ and represented with the letter C.
- *Spacecraft reference frame* (SRF): the traditional frame of reference fixed in the spacecraft's body, with origin at the SC's center. The $\boldsymbol{s}_3$ unit vector is orthogonal to the plane defined by the two OAs, $\boldsymbol{s}_1$ lies on the same plane and is defined as the bisectrix of the nominal inter-telescope angle. SRF is defined by the set $\{O_S, \boldsymbol{s}_1, \boldsymbol{s}_2, \boldsymbol{s}_3\}$ and represented with the letter S.
- Two *optical reference frames* (ORF): these have their origins at the OA's pivot point. The $\boldsymbol{o}_{1j}$ unit vector is directed along the longitudinal symmetry line of the telescope, $\boldsymbol{o}_{3j}$ is parallel to $\boldsymbol{s}_3$. They are defined by $\text{ORF}_j = \{O_{oj}, \boldsymbol{o}_{1j}, \boldsymbol{o}_{2j}, \boldsymbol{o}_{3j}\}$ and represented by the letter O_j.
- Two *test mass reference frames* (TMRF): these are the frames fixed with the two TMs' bodies and have their origins at the respective TMs' centers. The $\boldsymbol{m}_{1j}$ unit vector is directed out of the TM's surface that faces the drag free direction at working conditions, $\boldsymbol{m}_{3j}$ points out of the top surface. They are defined by $\text{TMRF}_j = \{O_{mj}, \boldsymbol{m}_{1j}, \boldsymbol{m}_{2j}, \boldsymbol{m}_{3j}\}$ and represented by the letter M_j.

It is useful to note that the ORFs are not just rotated by a fixed amount around the z axis with respect to the SRF; but instead they also include the additional rotation of the OAs with respect to their nominal positions 60° apart.

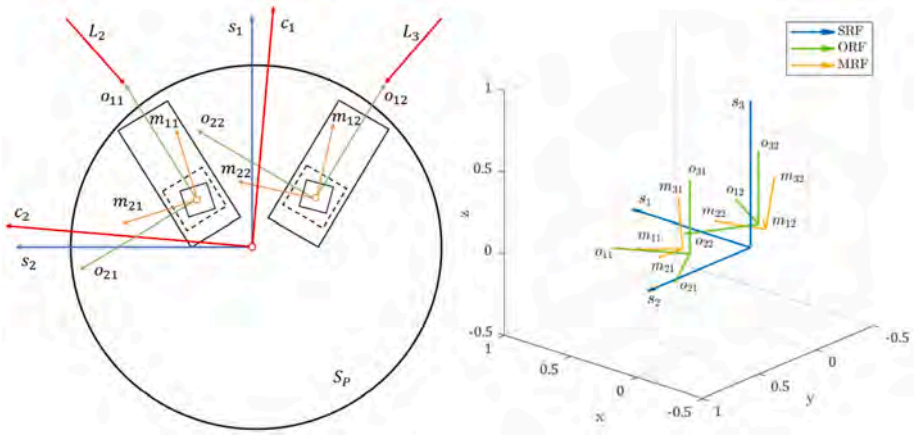

Fig. 18. LISA reference systems.

This total of seven different reference frames are either directly measurable or computable onboard. Specifically, the CRF should be computed by implementing the following algorithm (here assumed to be carried out on Spacecraft 1, without loss of generality):

1. *Laser beam vector*: in this step the unit vectors $\hat{\ell}_j^{\mathrm{S}}$ are computed starting from the measured azimuth α_j and elevation θ_j angles (measured by DWS). These unit vectors represent the direction of the incoming laser beams in the local SRF. The subscript j refers to the three different spacecrafts, that are numbered 1 to 3. Thus, for example, SC1 will receive lasers $\hat{\boldsymbol{\ell}}_2$ and $\hat{\boldsymbol{\ell}}_3$. Recalling that the azimuth angle is the rotation from $\boldsymbol{o}_2$ in the direction of $\boldsymbol{o}_1$ along the $\boldsymbol{o}_1$–$\boldsymbol{o}_2$ plane and elevation is the angle from the $\boldsymbol{o}_1$–$\boldsymbol{o}_2$ plane, positive towards the $\boldsymbol{o}_3$ direction; to derive the expression it is sufficient to apply the sequence of rotations to $\boldsymbol{o}_2$:

$$\mathrm{R} = \mathrm{R}_z(-\boldsymbol{\alpha}_j)\,\mathrm{R}_x(\boldsymbol{\theta}_j) = \begin{bmatrix} \boldsymbol{cos}(\boldsymbol{\alpha}_j) & \boldsymbol{sin}(\boldsymbol{\alpha}_j) & \mathbf{0} \\ -\boldsymbol{sin}(\boldsymbol{\alpha}_j) & \boldsymbol{cos}(\boldsymbol{\alpha}_j) & \mathbf{0} \\ \mathbf{0} & \mathbf{0} & \mathbf{1} \end{bmatrix} \begin{bmatrix} \mathbf{1} & \mathbf{0} & \mathbf{0} \\ \mathbf{0} & \boldsymbol{cos}(\boldsymbol{\theta}_j) & -\boldsymbol{sin}(\boldsymbol{\theta}_j) \\ \mathbf{0} & \boldsymbol{sin}(\boldsymbol{\theta}_j) & \boldsymbol{cos}(\boldsymbol{\theta}_j) \end{bmatrix} \tag{38}$$

$$\mathrm{l}_j^{\mathrm{O}_j} = \mathrm{R}o_2 = \begin{bmatrix} sin(\alpha_j)cos(\boldsymbol{\theta}_j) \\ cos(\alpha_j)cos(\boldsymbol{\theta}_j) \\ sin(\boldsymbol{\theta}_j) \end{bmatrix}, \tag{39}$$

$$\mathrm{l}_j^{\mathrm{S}} = \mathrm{T}_{\mathrm{O}_j}^{\mathrm{S}}\,\mathrm{l}_j^{\mathrm{O}_j}, \tag{40}$$

where $\mathrm{T}_{\mathrm{O}_j}^{\mathrm{S}}$ is the attitude direction cosine matrix of the spacecraft with respect to the j-th OA more details are given later.

2. *Constellation plane normal*: computes the orthogonal vector to the plane P containing both laser vectors. The orthogonal unitary vector is obtained by using the cross-product:

$$\boldsymbol{c}_3 = \frac{\hat{\boldsymbol{\ell}}_{\mathbf{3}}^{\mathrm{S}} \times \hat{\boldsymbol{\ell}}_{\mathbf{2}}^{\mathrm{S}}}{\left\| \hat{\boldsymbol{\ell}}_{\mathbf{3}}^{\mathrm{S}} \times \hat{\boldsymbol{\ell}}_{\mathbf{2}}^{\mathrm{S}} \right\|_2}, \tag{41}$$

then a unique plane P is defined by

$$\mathrm{P} = \left\{ \boldsymbol{x} \in \mathbb{R}^3 \mid \boldsymbol{c}_{\mathbf{3}}^{\top} \cdot \boldsymbol{x} = 0 \right\}. \tag{42}$$

Note that the order of the two vectors in the cross-product allows $\boldsymbol{c}_3$ to have a positive component along $\boldsymbol{s}_3$.

3. *Bisectrix computation*: the vector in plane P that bisects the angle between $\hat{\ell}_{\mathbf{2}}^{\mathrm{S}}$ and $\hat{\ell}_{\mathbf{3}}^{\mathrm{S}}$ can be found by noticing that both the laser vectors are unit vectors, thus, they constitute the edges of an isosceles triangle, that has its main vertex in the origin. Therefore, $\boldsymbol{c}_1$ can be computed by finding the mid-point of the basis of the triangle and then normalizing it:

$$\Delta\hat{\ell} = \hat{\ell}_{\mathbf{2}}^{\mathrm{S}} - \hat{\ell}_{\mathbf{3}}^{\mathrm{S}}, \text{basis segment}, \tag{43}$$

$$\hat{\ell}_{\mathrm{M}} = \hat{\ell}_{\mathbf{3}}^{\mathrm{S}} + \frac{1}{2}\Delta\hat{\ell} = \frac{1}{2}\hat{\ell}_{\mathbf{2}}^{\mathrm{S}} + \frac{1}{2}\hat{\ell}_{\mathbf{3}}^{\mathrm{S}}, \text{mid} - \text{point}, \tag{44}$$

$$\boldsymbol{c}_{\mathbf{1}} = \frac{\hat{\ell}_{\mathrm{M}}}{\|\hat{\ell}_{\mathrm{M}}\|} = \frac{\hat{\boldsymbol{\ell}}_{\mathbf{2}}^{\mathrm{S}} + \hat{\boldsymbol{\ell}}_{\mathbf{3}}^{\mathrm{S}}}{\left\| \hat{\boldsymbol{\ell}}_{\mathbf{2}}^{\mathrm{S}} + \hat{\boldsymbol{\ell}}_{\mathbf{3}}^{\mathrm{S}} \right\|_2}. \tag{45}$$

4. *Remaining axis*: the remaining unit vector $\boldsymbol{c}_2$ is obtained by requiring the frame to be right-handed, i.e., $\boldsymbol{c}_2 = \boldsymbol{c}_3 \times \boldsymbol{c}_1$, where $\boldsymbol{c}_1$ and $\boldsymbol{c}_3$ were computed in the previous steps.

References

[1] K. Danzmann and the LISA Study Team, LISA: laser interferometer space antenna for gravitational wave measurements, Classical Quant. Grav. 13 (11A) (1996) A247.

[2] D. Shaddock, Space-based gravitational wave detection with lisa, Classical Quant. Grav. 25 (11) (2008), 114012.

[3] L. Giulicchi, S.-F. Wu, T. Fenal, Attitude and orbit control systems for the LISA pathfinder mission, Aero. Sci. Technol. 24 (1) (2013) 283–294.

[4] P. Amaro-Seoane, H. Audley, S. Babak, J. Baker, E. Barausse, P. Bender, E. Berti, P. Bi- netruy, M. Born, D. Bortoluzzi, et al., Laser Interferometer Space Antenna, 2017 arXiv preprint arXiv:1702.00786.

[5] P. Touboul, B. Foulon, M. Rodrigues, J. Marque, In orbit nano-g measurements, lessons for future space missions, Aero. Sci. Technol. 8 (5) (2004) 431–441.

[6] S. Vidano, C. Novara, M. Pagone, J. Grzymisch, The LISA DFACS: model predictive control design for the test mass release phase, Acta Astronaut. 193 (2022) 731–743.

[7] S. Vidano, C. Novara, L. Colangelo, J. Grzymisch, The LISA DFACS: a nonlinear model for the spacecraft dynamics, Aero. Sci. Technol. 107 (2020).

[8] X. Lian, J. Zhang, L. Lu, J. Wang, L. Liu, J. Sun, Y. Sun, Frequency separation control for drag-free satellite with frequency-domain constraints, IEEE Trans. Aero. Electron. Syst. 57 (6) (2021) 4085–4096.

[9] G.D. Racca, P.W. McNamara, The LISA pathfinder mission, Space Sci. Rev. 151 (1) (2010) 159–181.

[10] P. McNamara, S. Vitale, K. Danzmann, L.P.S.W. Team, et al., LISA pathfinder,, Classical Quant. Grav. 25 (11) (2008), 114034.

[11] M. Armano, M. Benedetti, J. Bogenstahl, D. Bortoluzzi, P. Bosetti, N. Brandt, A. Cav- alleri, G. Ciani, I. Cristofolini, A. Cruise, et al., LISA pathfinder: the experiment and the route to lisa, Classical Quant. Grav. 26 (9) (2009), 094001.

[12] J. Thorpe, T. Littenberg, J. Baker, J. Slutsky, et al., LISA pathfinder as a micrometeoroid instrument, in: Journal of Physics: Conference Series, vol. 840, IOP Publishing, 2017, 012007 no. 1.

[13] J.I. Thorpe, J. Slutsky, J.G. Baker, T.B. Littenberg, S. Hourihane, N. Pagane, P. Pokorny, D. Janches, M. Armano, H. Audley, et al., Micrometeoroid events in LISA pathfinder, Astrophys. J. 883 (1) (2019) 53.

[14] S. Vargas, H.M. Becerra, J.-B. Hayet, Mpc-based distributed formation control of multiple quadcopters with obstacle avoidance and connectivity maintenance, Control Eng. Pract. 121 (2022), 105054.

[15] F. Cirillo, P.F. Gath, Control system design for the constellation acquisition phase of the LISA mission, in: Journal of Physics: Conference Series, vol. 154, IOP Publishing, 2009, 012014 no. 1.

[16] M. Virdis, S. Vidano, M. Pagone, D. Ruggiero, C. Novara, J. Grzymisch, V. Preda, E. Punta, The LISA DFACS: effects of micrometeoroid impacts in the drag-free mode, in: IAC Conference, 2021.

[17] J. White, Meteoric effects on attitude control of space vehicles, ARS J. 32 (1) (1962) 75–78.

[18] G.J. Cloutier, Attitude perturbation of space vehicles by meteoroid impacts, J. Spacecraft Rockets 3 (4) (1966) 523–530.

[19] R. Eichelberger, J. Gehring, Effects of meteoroid impacts on space vehicles, ARS J. 32 (10) (1962) 1583–1591.

[20] R. Putzar, E. Watson, M. Schimmerohn, P. Kärräng, M. Millinger, How hypervelocity impacts can affect the LISA mission–the mirad study, in: International Astronautical Congress. Washington, DC, 2019.

[21] R. Arrell, N.J. Kasdin, Reorientation of rotating deep space tethered constellations, in: AIAA Guidance, Navigation, and Control Conference and Exhibit, 2003, p. 5367.

[22] B. Li, Y. Wang, K. Zhang, G.-R. Duan, Constrained feedback control for space- craft reorientation with an optimal gain, IEEE Trans. Aero. Electron. Syst. 57 (6) (2021) 3916–3926.

[23] L. Appel, M. Guelman, D. Mishne, Optimization of satellite constellation reconfiguration maneuvers, Acta Astronaut. 99 (2014) 166–174.

[24] M. Boggio, L. Colangelo, M. Virdis, M. Pagone, C. Novara, Earth gravity in-orbit sensing: mpc formation control based on a novel constellation model, Rem. Sens. 14 (2022) 2815.

[25] Y. Zou, K. Xia, W. He, Adaptive fault-tolerant distributed formation control of clustered vertical takeoff and landing uavs, IEEE Trans. Aero. Electron. Syst. 58 (2) (2021) 1069–1082.

[26] E. Hill, S.A. Gadsden, M. Biglarbegian, Explicit nonlinear mpc for fault tolerance using interacting multiple models, IEEE Trans. Aero. Electron. Syst. 57 (5) (2021) 2784–2794.

[27] H. Park, Y. Kim, Adaptive fault tolerant flight control for input redundant systems using a nonlinear reference model, IEEE Trans. Aero. Electron. Syst. 57 (5) (2021) 3337–3356.

[28] X. Sun, X. Mao, P. Chen, High-precision attitude determination using spaceborne gravity gradiometer and gyroscope, Acta Astronaut. 200 (2022) 213–225.

[29] Q. Dang, K. Liu, J. Wei, Explicit reference governor based spacecraft attitude reorientation control with constraints and disturbances, Acta Astronaut. 190 (2022) 455–464.

[30] Y. Zivan, D. Choukroun, Dual quaternion kalman filtering and observability analysis for satellite relative navigation with line-of-sight measurements, IEEE Trans. Aero. Electron. Syst. 58 (2) (2021) 754–765.

[31] C. Nainer, H. Garnier, M. Gilson, H. Evain, C. Pittet, Parameter estimation of a gyroless micro-satellite from telemetry data, Control Eng. Pract. 123 (2022), 105134.

[32] A. Fiot, S. Changey, N. Petit, Attitude estimation for artillery shells using magnetometers and frequency detection of accelerometers, Control Eng. Pract. 122 (2022), 105080.

[33] S.H. Pourtakdoust, M.F. Mehrjardi, M. Hajkarim, Attitude estimation and control based on modified unscented kalman filter for gyro-less satellite with faulty sensors, Acta Astronaut. 191 (2022) 134–147.

[34] S. Dionisio, S. Cesare, F. Basile, L. Garin, A LISA mission simulation environment: Tas numes simulator framework a powerful tool for future missions, in: 11th International ESA Conference on Guidance, Navigation & Control Systems, 2021.

[35] S.K. Spurgeon, Sliding Mode Observers - Historical Background and Basic Introduction, 2015.

[36] S. Na, L. Librescu, M.-H. Kim, I.-J. Jeong, P. Marzocca, Robust aeroelastic control of flapped wing systems using a sliding mode observer, Aero. Sci. Technol. 10 (2) (2006) 120–126.

[37] A. Levant, Robust exact differentiation via sliding mode technique, Automatica 34 (3) (1998) 379–384 [Online]. Available: https://www.sciencedirect.com/science/article/pii/S0005109897002094.

[38] J. Picó, E. Picó-Marco, A. Vignoni, H. De Battista, Stability preserving maps for finite-time convergence: super-twisting sliding-mode algorithm, Automatica 49 (2) (2013) 534–539 [Online]. Available: https://www.sciencedirect.com/science/article/pii/S0005109812005584.

[39] S.V. Gutierrez, C. Zhang, J. de León-Morales, F. Plestan, A simplified version of adaptive super twisting—application to the control of floating wind turbine, Control Eng. Pract. 125 (2022), 105208.

[40] P. Morga, M. Mancini, E. Capello, Flexible spacecraft model and robust control techniques for attitude maneuvers, in: 2022 American Control Conference, *ACC)*. IEEE, 2022, pp. 1120–1126.